

**MASARYKOVA UNIVERZITA**  
**PŘÍRODOVĚDECKÁ FAKULTA**  
ÚSTAV TEORETICKÉ FYZIKY A ASTROFYZIKY

# **Diplomová práce**

**BRNO 2020**

**JIŘÍ ŽÁK**

**M A S A R Y K O V A**  
**U N I V E R Z I T A**  
**PŘÍRODOVĚDECKÁ FAKULTA**  
ÚSTAV TEORETICKÉ FYZIKY A ASTROFYZIKY

---

# **Detekce atmosfér exoplanet**

Diplomová práce

**Jiří Žák**

**Vedoucí práce: Mgr. Marek Skarka, Ph.D.      Brno 2020**

# Bibliografický záznam

<b>Autor:</b>	Jiří Žák Přírodovědecká fakulta, Masarykova univerzita Ústav teoretické fyziky a astrofyziky
<b>Název práce:</b>	Detekce atmosfér exoplanet
<b>Studijní program:</b>	Teoretická fyzika a astrofyzika
<b>Studijní obor:</b>	Astrofyzika
<b>Vedoucí práce:</b>	Mgr. Marek Skarka, Ph.D.
<b>Akademický rok:</b>	2019/2020
<b>Počet stran:</b>	X + 51
<b>Klíčová slova:</b>	exoplanety, exoatmosféry, transmisní spektroskopie, sodík

# Bibliographic Entry

**Author:** Jiří Žák  
Faculty of Science, Masaryk University  
Department of Theoretical Physics and Astrophysics

**Title of Thesis:** Detection of exoplanetary atmospheres

**Degree Programme:** Theoretical Physics and Astrophysics

**Field of Study:** Astrophysics

**Supervisor:** Mgr. Marek Skarka, Ph.D.

**Academic Year:** 2019/2020

**Number of Pages:** X + 51

**Keywords:** Exoplanets, Exoatmospheres, transmission spectroscopy, sodium

# Abstrakt

Metodou transmisní spektroskopie můžeme studovat chemické složení atmosfér tranzitujících exoplanet. To nám dovoluje studovat fyzikálně-chemické procesy v exoplanetárních atmosférách a umožňuje lépe porozumět formaci a evoluci planet. V této práci jsme zkoumali archivní spektroskopická data planet WASP-76b, WASP-127b, WASP-166b a KELT-11b z přístroje High Accuracy Radial velocity Planet Searcher (HARPS). Porovnáním dat pořízených před a po tranzitu s daty pořízenými během tranzitu jsme získali spektrum planety bez přítomnosti stelárního spektra. Zkoumali jsme přítomnost sodíku (sodíkový dublet), vodíku ( $H\alpha$ ,  $H\beta$ ) a lithia (670.8 nm). Vliv hvězdné aktivity jsme monitorovali za použití Mg I a Ca I čar. Hlavním výsledkem práce je detekce sodíku v atmosféře planety WASP-76b na úrovni  $7\text{--}9\sigma$ . V atmosféře WASP-127b jsme detekovali sodík na úrovni  $4\text{--}8\sigma$ , čímž jsme nezávisle potvrdili přítomnost sodíku dříve zjištěnou metodou nízkodisperzní spektroskopie. Atmosféry planet KELT-11b a WASP-166b nevykazují přítomnost sodíku ani jiného zkoumaného prvku, což může být způsobeno hustými mraky ve vysokých vrstvách atmosféry. Na závěr jsme popsali dva připravované projekty pro další výzkum exoatmosfér.

# Abstract

The technique of transmission spectroscopy allows us to constrain the chemical composition of the atmospheres of transiting exoplanets. This gives us the chance to study the physicochemical processes in the exoplanetary atmospheres and improve our understanding of the formation and evolution of planets. We analyzed archival High Accuracy Radial velocity Planet Searcher (HARPS) spectroscopic time series of four exoplanets, namely WASP-76b, WASP-127b, WASP-166b, and KELT-11b, searching for traces of sodium (sodium doublet), hydrogen ( $H\alpha$ ,  $H\beta$ ), and lithium (670.8 nm). Simultaneously, the stellar activity was monitored using the Mg I and Ca I lines. We detected sodium in the atmosphere of WASP-76b at a  $7\text{--}9\sigma$  level. Furthermore, we also report the detection of sodium in the atmosphere of WASP-127b at a  $4\text{--}8\sigma$  level of significance, confirming earlier results based on low-resolution spectroscopy. The data show no sodium nor any other studied element at high confidence levels for WASP-166b nor KELT-11b, hinting at the presence of thick high clouds. We finish with an outlook on how we want to move forward with exoatmosphere characterization by introducing two feasible projects in the near future.

ZADÁNÍ  
DIPLOMOVÉ PRÁCE

Akademický rok: 2019/2020

Ústav:	Ústav teoretické fyziky a astrofyziky
Student:	Bc. Jiří Žák
Program:	Fyzika
Obor:	Teoretická fyzika a astrofyzika
Směr:	Astrofyzika

Ředitel Ústavu teoretické fyziky a astrofyziky PřF MU Vám ve smyslu Studijního a zkušebního řádu MU určuje diplomovou práci s názvem:

Název práce:	Detekce atmosfér exoplanet
Název práce anglicky:	Detection of exoplanetary atmospheres
Jazyk závěrečné práce:	

**Oficiální zadání:**

With the state-of-the-art instruments and telescopes, astronomers are currently able not only detect and study exoplanets but also study their atmospheres. The aim of the project is to use archival high-resolution spectra from the ESO archive and search for signatures of the exoatmospheres using the method of transmission spectroscopy.

Vedoucí práce:	Mgr. Marek Skarka, Ph.D.
Konzultant:	Bc. Petr Kabáth, Dr. rer. nat.
Datum zadání práce:	6. 12. 2018
V Brně dne:	16. 3. 2020

Souhlasím se zadáním (podpis, datum):

.....  
Bc. Jiří Žák  
student

.....  
Mgr. Marek Skarka, Ph.D.  
vedoucí práce

.....  
prof. Rikard von Unge, Ph.D.  
ředitel Ústavu teoretické fyziky a  
astrofyziky

# Acknowledgement

I would like to thank Dr. Petr Kabáth, Dr. Henri Boffin and Dr. Valentin Ivanov for their valuable advices and encouragement. I am also grateful to Dr. Marek Skarka for his numerous and valuable comments and suggestions to improve this thesis. I would like to thank them also for reading my works and proposals which were often far from being perfect. Their continous support has allowed me to scientifically grow.

# Prohlášení

Prohlašuji, že jsem svoji diplomovou práci vypracoval samostatně pod vedením vedoucího práce s využitím informačních zdrojů, které jsou v práci citovány.

Brno 20. května 2020

.....  
Jiří Žák



# Contents

<b>Chapter 1. Introduction</b>	<b>1</b>
1.1 Exoplanets	1
1.2 Exoatmospheres	4
1.2.1 Composition of planetary atmospheres in our Solar system	7
1.3 Transmission spectroscopy	8
1.3.1 Low-resolution transmission spectroscopy	9
1.3.2 High-resolution transmission spectroscopy	11
1.3.3 High-resolution spectrographs	13
<b>Chapter 2. Exoatmosphere detectability and target selection</b>	<b>16</b>
2.1 Target selection	17
2.1.1 WASP-76b	18
2.1.2 WASP-127b	18
2.1.3 KELT-11b	18
2.1.4 WASP-166b	19
<b>Chapter 3. Data sets and Analysis</b>	<b>20</b>
3.1 Data sets	20
3.2 Data reduction	20
3.3 Normalization	22
3.4 Telluric correction	23
3.5 Rossiter-McLaughlin effect	23
3.6 Transmission spectrum	25
3.7 Stellar activity	25
<b>Chapter 4. Results and discussion</b>	<b>27</b>
4.1 WASP-76b	27
4.2 WASP-127b	29
4.3 WASP-166b	30
4.4 KELT-11b	30
4.5 Discussion	31
<b>Chapter 5. Future prospects</b>	<b>33</b>
5.1 Future projects	33

5.2 Future plans . . . . .	37
<b>Chapter 6. Conclusions . . . . .</b>	<b>40</b>
<b>References . . . . .</b>	<b>42</b>

# Chapter 1

## Introduction

### 1.1 Exoplanets

Exoplanets are planets outside of our Solar system. They are objects with masses below  $M_p = 13 M_{\text{Jup}}$ <sup>1</sup>, thus, have never started nuclear fusion (Perryman, 2018). One of the first modern papers about the detection of exoplanets was published by Strand (1943) who reported a companion around a system 61 Cyg using the astrometric method (a precise measurement of stars' position on the sky), however a study by Heintz (1978) disproved this discovery. Later, Struve (1952) proposed to use Doppler spectroscopy and transit method to detect hot Jupiters<sup>2</sup> on short orbits. Latham, et al. (1989) reported a discovery of an object orbiting a star HD 114762. They determined a bottom mass limit of the companion as  $M_c = 11 M_{\text{Jup}}$ , however, due to the unknown inclination they preferred an explanation with a non-planetary companion. Campbell, Walker & Yang (1988) mentioned the possibility of a Jupiter-size planet around Gamma Cep, however, later Walker, et al. (1992) argued that Gamma Cep is more likely a radial velocity variable star<sup>3</sup>. The same year, first firm detection of an exoplanet around pulsar PSR 1257+12 was reported (Wolszczan & Frail, 1992). The first exoplanet around a main-sequence star was discovered in 1995 (Mayor & Queloz, 1995). They used the radial velocity method to detect a hot Jupiter orbiting star 51 Peg using data from ELODIE spectrograph mounted on the 1.9-m telescope at the Observatory Haute-Provence in France. This accomplishment was awarded the Nobel prize in 2019. It took another 4 years from their discovery for a transit detection of the first exoplanet, when Henry, et al. (2000) and Charbonneau, et al. (2000) detected transit of HD 209458b. Since these discoveries, research of exoplanets has become one of the frontiers of today's astronomy.

In the early days, exoplanets were discovered from the ground and most of them were hot Jupiters. Their short orbital periods, high masses, and large diameters make them ideal targets for the Doppler spectroscopy, as well as for the transit method. Doppler spectroscopy is an indirect method for discovering exoplanets and other objects; it measures

---

<sup>1</sup>An alternative definition was proposed by Hatzes & Rauer (2015) based on the changes of the slope in the mass – density relationship. They proposed a new definition of a planet, extending the planetary mass up to  $M_p = 60 M_{\text{Jup}}$ .

<sup>2</sup>Jupiter-size exoplanet close to their star.

<sup>3</sup>Hatzes, et al. (2003) showed that Gamma Cep has a planetary companion.

radial velocity shift that is caused by the orbital motion. An early work was done by [Griffin \(1973\)](#) who discussed the possibility of determining the radial velocities to a precision of  $10 \text{ ms}^{-1}$ , sufficient to detect exoplanets. This method was later advanced by [Campbell, Walker & Yang \(1988\)](#); [Hatzes & Cochran \(1992\)](#); [Butler, et al. \(1996\)](#) and others to enable very precise measurements of radial velocities that led to several discoveries of exoplanets ([Butler, et al., 2017](#)).

The transit method measures the drops in brightness while the planet is in front of the parents star's disk. One of the first space missions dedicated to exoplanets was *CoRoT* ([Baglin, et al., 2002](#)) that was launched in 2006. It led to the discoveries of 32 transiting exoplanets, whose radiuses and masses were later determined. After a very successful mission, *CoRoT* retired in 2012.

A truly revolutionary mission was *Kepler* ([Borucki, et al., 2010](#)), which led to the discoveries of thousands of transiting exoplanets and provided us with exceptionally accurate light curves. However, most of the *Kepler*'s targets are too faint for ground-based spectroscopic follow-up observations. The Transiting Exoplanet Survey Satellite (*TESS*) mission ([Ricker, et al., 2015](#)), that was launched in 2018, is providing suitable targets for the follow-up observations especially regarding bright targets for exoatmosphere characterization ([Jones, et al., 2019](#); [Dumusque, et al., 2019](#)). In addition, ground-based photometric surveys, e.g. WASP ([Pollacco, et al., 2006](#)), KELT ([Pepper, et al., 2007](#)), HAT ([Bakos, et al., 2004](#)), MASCARA ([Snellen, et al., 2012](#)), and others, have provided candidates for exoatmosphere detection as they have discovered hundreds of planets orbiting bright stars. The PLAnetary Transits and Oscillations of stars (*PLATO*) mission ([Rauer, et al., 2016](#)), that is set to launch in 2026, will discover thousands of exoplanets using transit method and provide a large number of candidates for transmission spectroscopy.

Besides doppler spectroscopy and transit method, exoplanets were detected using various methods including direct imaging ([Marois, et al., 2008](#)), astrometry ([Wertz, et al., 2017](#)), gravitational microlensing ([Beaulieu, et al., 2006](#)), transit timing variations ([Ballard, et al., 2011](#)), and others. As of today<sup>4</sup>, we currently know more than 4265 exoplanets ([exoplanet.eu](#), [Schneider, et al., 2011](#)). A thorough overview of major exoplanetary discoveries throughout history can be found in [Perryman \(2018\)](#). We present a mass – orbital period diagram of known exoplanets in Fig. 1.1. As can be seen, the plot is dominated by giant planets. The left quarter of the graph contains many more planets however without mass determination (from *Kepler* and other photometric missions). For planets without radius determination, it is possible to use calibrated mass-radius relations to get radius estimation (Fig. 1.2, [Bashi, et al., 2017](#); [Otegi, Bouchy & Helled, 2020](#)). From the Fig. 1.2, it can be seen that the size of giant planets nearly does not depend on their mass.

---

<sup>4</sup>May 31, 2020

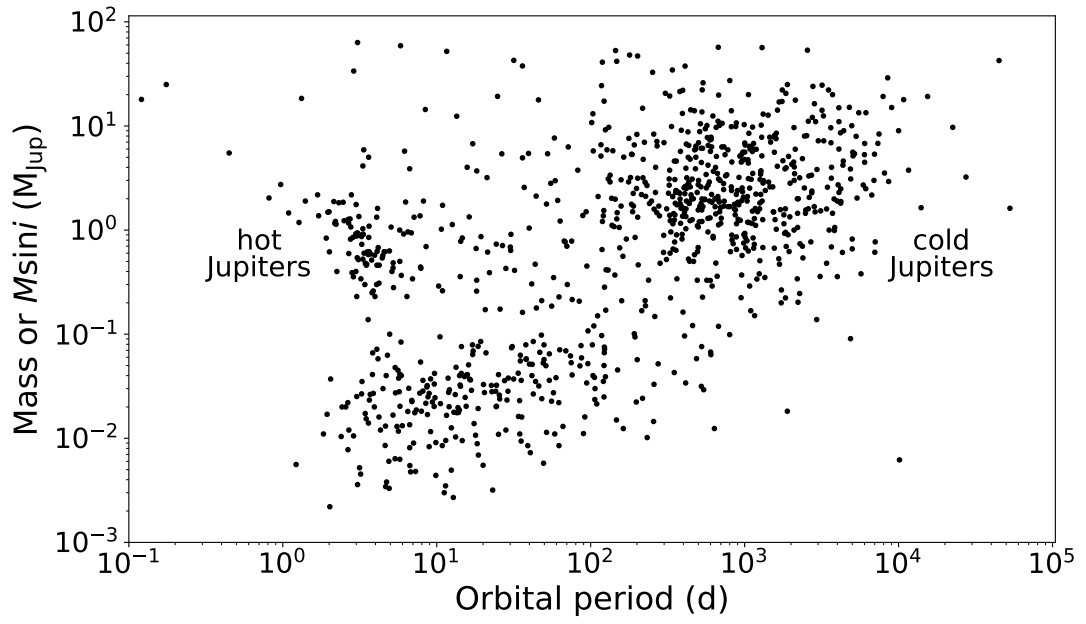


Figure 1.1: Mass – orbital period diagram of confirmed exoplanets. Only planets with mass determinations are shown. Data from exoplanet.eu database ([Schneider, et al., 2011](#)).

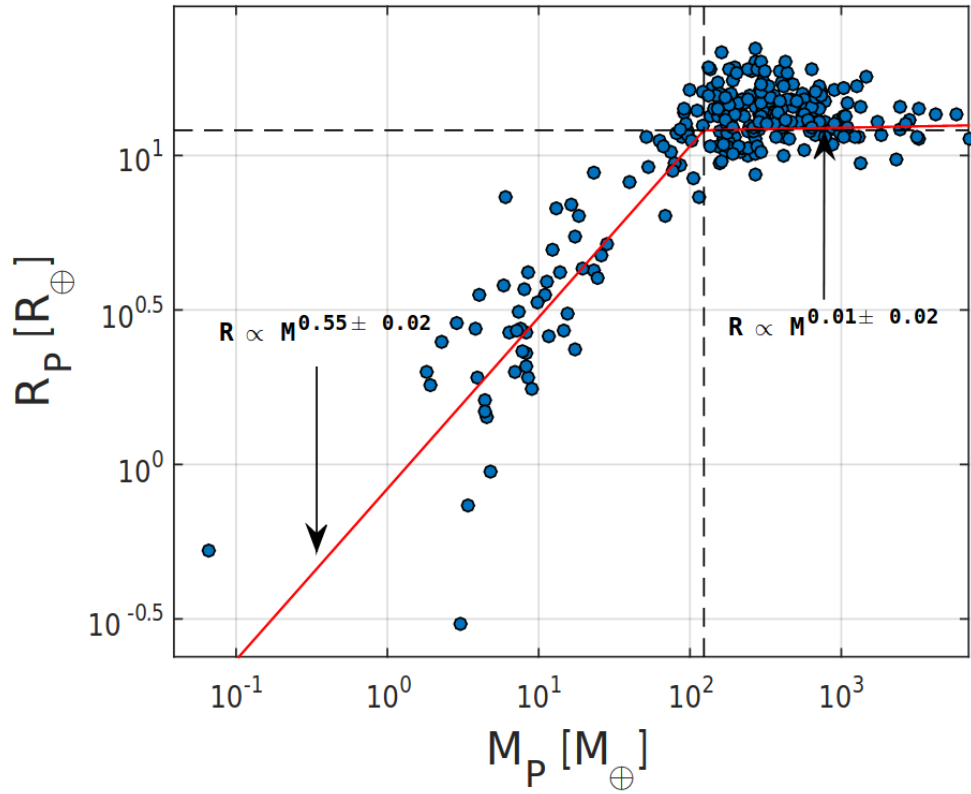


Figure 1.2: The radius–mass diagram and the derived best-fit curves, and mass-radius relations for small and giant planets ([Bashi, et al., 2017](#)).

## 1.2 Exoatmospheres

Exoplanetary atmospheres are atmospheres of exoplanets. One of the very first studies on exoatmospheres was the theoretical work by [Seager & Sasselov \(2000\)](#) where they discuss the possibility of detecting exoatmosphere using transmission spectroscopy. They elaborate that alkali metals, e.g. sodium and potassium, are very suitable for detection due to strong and sharp absorption profiles. Their ideas were subsequently supported by [Charbonneau, et al. \(2002\)](#) whose discovery of sodium presence in the atmosphere of HD 209458b using the Hubble Space Telescope (*HST*) was the first confirmed detection of the exoatmosphere. First ground-based detections of exoatmosphere were made by [Snellen, et al. \(2008\)](#) and [Redfield, et al. \(2008\)](#) as they detected sodium in the atmospheres of HD 209458b and HD 189733b using the 8.2-m Subaru and the 9.2-m Hobby-Eberly telescope. [Wyttenbach, et al. \(2015\)](#) detected sodium using the 3.6-m telescope with the The High Accuracy Radial Velocity Planet Searcher (HARPS) instrument. This was the first ground-based detection with a 4-m class telescope. We present a short overview of detected atoms and molecules in Table 1.1. Sodium and potassium have been detected with great success in the optical due to their strong and sharp profiles. In the infra-red (IR) region, water vapor and methane bands have been detected due to their strong absorption profile that consists of many individual lines. For the planets with temperature higher than 2000 K, TiO, VO and AlO have been detected.

Nowadays, hot Jupiters<sup>5</sup> are the most frequently studied planets for exoatmosphere characterization. It is due to the number of such known planets, their high temperature and large size. Current challenge is to explain the large diversity of their atmospheres. Fig. 1.3 shows 3 temperature profiles which can arise as a result of atmospheric processes. A profile of highly-irradiated planet with thermal inversion is shown in red. Thermal inversions are regions of the atmosphere where the temperature increases with altitude ([Gandhi & Madhusudhan, 2019](#)). Their origin is due to the presence of strong UV/visible absorption of the stellar irradiation. In hot Jupiters, the absorption can be caused by molecules, such as TiO and VO ([Hubeny, Burrows & Sudarsky, 2003](#)). In cyan, a profile of irradiated planet without thermal inversion is shown in Fig. 1.3. Finally, the grey dashed line displays a profile of a weakly irradiated planet.

Furthermore, a number of atmospheric processes are seen in the exoatmospheres. As can be expected, atmospheric escape is occurring at very low pressures in the highest levels of the atmosphere. Below that highest level of the atmosphere, the low density and high radiation field causes photochemical processes, e.g., photodissociation of prominent molecules into atomic species and formation of new ones. Further down in the atmosphere, clouds/hazes and temperature inversions occur. These processes are closely related to the atmospheric chemical composition. Finally, deep in the atmosphere, the pressure and temperature are high enough that chemical equilibrium can prevail.

Each region of the atmosphere can be used to study specific physicochemical processes and different chemical species and regions of the atmosphere can be probed in different parts of the electromagnetic spectrum. Molecules (e.g. H<sub>2</sub>O, CO, CO<sub>2</sub>, CH<sub>4</sub>) absorb primarily in the infrared due to rotational and vibrational transitions with the exception of some metal molecules (TiO, VO) which can also have a strong absorption in the

---

<sup>5</sup>The atmospheres of mini-Neptunes and super-Earths were also investigated (e.g., [Benneke, et al., 2019](#)).

Table 1.1: Overview of detected atmospheric signatures.

Element	Planet
Na	HD 189733b <sup>1</sup> , WASP-127b <sup>2</sup> , WASP-52b <sup>3</sup> , WASP-49b <sup>4</sup> , HD 209458b <sup>5</sup> WASP-69b <sup>6</sup> , WASP-39b <sup>7</sup> , WASP-96b <sup>8</sup> , WASP-17b <sup>9</sup> , XO-2b <sup>10</sup> ,
K	WASP-6b <sup>11</sup> , WASP-31b <sup>12</sup> , WASP-39b <sup>13</sup> , WASP-127b <sup>2</sup> XO-2b <sup>10</sup> , HD 80606b <sup>14</sup>
Li	WASP-127b <sup>2</sup>
TiO	WASP-19b <sup>15</sup> , WASP-33b <sup>16</sup>
VO	WASP-121b <sup>17</sup>
AlO	WASP-33b <sup>18</sup>
Fe	KELT-9b <sup>19</sup>
Sc	HD 209458b <sup>20</sup>
Si	HD 209458b <sup>21</sup>
Ti, Ti+	KELT-9b <sup>19</sup>
H	HD 189733b <sup>22</sup> , HD 209458b <sup>23</sup> , GJ 436b <sup>24</sup> , WASP-52b <sup>3</sup>
H <sub>2</sub> O	HD 189733b <sup>25</sup> , HD 209458b <sup>26</sup> , WASP-12b <sup>27</sup> , WASP-17b <sup>28</sup> , WASP-19b <sup>29</sup> , WASP-39b <sup>30</sup> , WASP-43b <sup>31</sup> , WASP-63b <sup>32</sup> WASP-121b <sup>33</sup> , HAT-P-1b <sup>34</sup> , HAT-P-11b <sup>35</sup> , HAT-P-26b <sup>36</sup> , HAT-P-32b <sup>37</sup> , XO-1b <sup>26</sup>
He	WASP-107b <sup>38</sup> , GJ 3470 <sup>39</sup> , HD 189733b <sup>40</sup> , WASP-69b <sup>41</sup>
CO	WASP-18b <sup>42</sup> , HR 8799c <sup>43</sup> , 51 Peg b <sup>44</sup>
HCN	HD 209458b <sup>45</sup>
NH <sub>3</sub>	HD 209458b <sup>46</sup>
CH <sub>4</sub>	HR 8799b <sup>47</sup> , 51 Eri b <sup>48</sup> , GJ 504b <sup>49</sup> ,

**References:** <sup>1</sup>Redfield, et al. (2008), <sup>2</sup>Chen, et al. (2018), <sup>3</sup>Chen, et al. (2020),  
<sup>4</sup>Wyttenbach, et al. (2017), <sup>5</sup>Charbonneau, et al. (2002), <sup>6</sup>Casasayas-Barris, et al. (2017),  
<sup>7</sup>Nikolov, et al. (2016), <sup>8</sup>Nikolov, et al. (2018), <sup>9</sup>Sing, et al. (2016), <sup>10</sup>Sing, et al. (2012),  
<sup>11</sup>Carter, et al. (2020), <sup>12</sup>Sing, et al. (2015), <sup>13</sup>Fischer, et al. (2016), <sup>14</sup>Colón, et al. (2012),  
<sup>15</sup>Sedaghati, et al. (2017), <sup>16</sup>Haynes, et al. (2015), <sup>17</sup>Evans, et al. (2017), <sup>18</sup>von Essen, et  
al. (2019), <sup>19</sup>Hoeijmakers, et al. (2018), <sup>20</sup>Astudillo-Defru & Rojo (2013), <sup>21</sup>Schlawin, et  
al. (2010), <sup>22</sup>Bourrier, et al. (2013), <sup>23</sup>Vidal-Madjar, et al. (2003), <sup>24</sup>Ehrenreich, et al.  
(2015), <sup>25</sup>McCullough, et al. (2014), <sup>26</sup>Deming, et al. (2013), <sup>27</sup>Kreidberg, et al. (2015),  
<sup>28</sup>Mandell, et al. (2013), <sup>29</sup>Huitson, et al. (2013), <sup>30</sup>Wakeford, et al. (2018), <sup>31</sup>Kreidberg,  
et al. (2014), <sup>32</sup>Kilpatrick, et al. (2018), <sup>33</sup>Evans, et al. (2016), <sup>34</sup>Wakeford, et al. (2013),  
<sup>35</sup>Fraine, et al. (2014), <sup>36</sup>Wakeford, et al. (2017a), <sup>37</sup>Damiano, et al. (2017), <sup>38</sup>Spake, et  
al. (2018), <sup>39</sup>Palle, et al. (2020), <sup>40</sup>Salz, et al. (2018), <sup>41</sup>Nortmann, et al. (2018),  
<sup>42</sup>Sheppard, et al. (2017), <sup>43</sup>Konopacky, et al. (2013), <sup>44</sup>Brogi, et al. (2013), <sup>45</sup>Hawker, et  
al. (2018), <sup>46</sup>MacDonald & Madhusudhan (2017), <sup>47</sup>Barman, et al. (2015), <sup>48</sup>Samland, et  
al. (2017), <sup>49</sup>Janson, et al. (2013)

visible spectrum. Atomic species (e.g., Na, K, Fe, O) absorb primarily in the optical and UV (in higher atmospheric layers, [Madhusudhan, 2019](#)). Thus, it is beneficial to use multiwavelength observations to investigate various layers of the atmosphere.

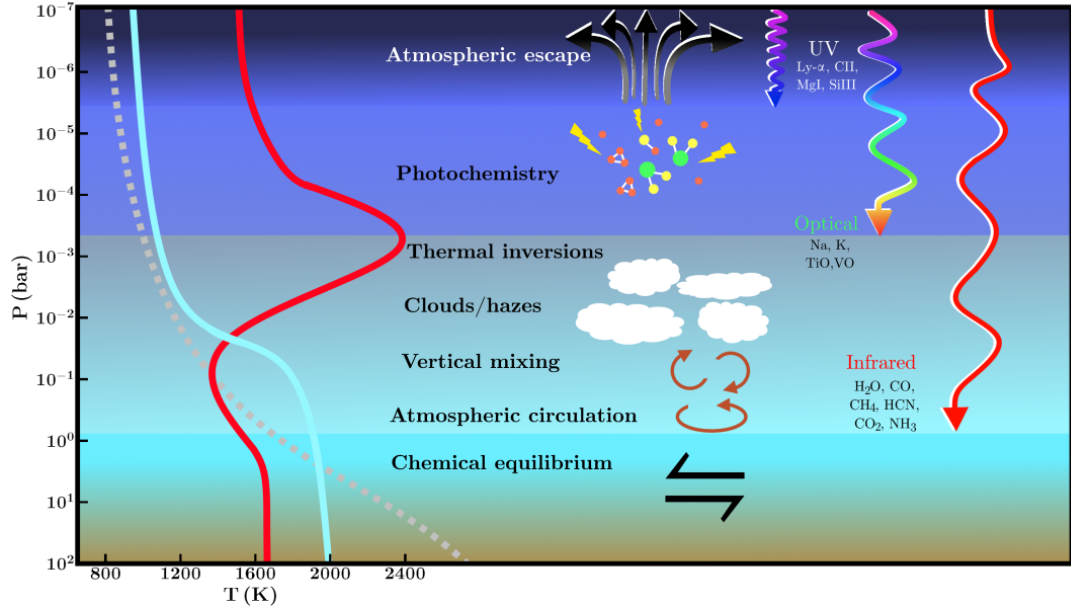


Figure 1.3: The temperature – pressure profile for exoplanetary atmosphere ([Madhusudhan, 2019](#)). Three profiles are shown: a profile of a highly-irradiated planet with thermal inversion (red), a profile of irradiated planet without thermal inversion (cyan) and a profile of a weakly irradiated planet. See the text for more details.

Two successful methods to detect exoplanetary atmospheres are transit spectroscopy and direct imaging ([Marois, et al., 2008](#)). Transit spectroscopy allows three configurations to observe planetary atmosphere: (a) a transmission spectroscopy when the planet is in front of the host star ([Wytenbach, et al., 2015](#))<sup>6</sup>, (b) an emission spectrum as the planet passes behind the host star during secondary eclipse ([Haynes, et al., 2015](#)), and (c) a phase curve as the planet orbits between the primary and secondary eclipses ([Stevenson, et al., 2014](#)).

Direct imaging relies on obtaining a planetary spectrum directly by blocking the stellar light using a coronagraph. The requirements for the sensitivity are very challenging in the optical to detect an exoplanet. Furthermore, adaptive optics is more accessible in the IR region so it is beneficial to perform direct imaging in the IR region. In comparison to transmission spectroscopy, this method is suitable for young giant planets with high temperatures at large orbital separations. By obtaining thermal emission spectra, atmospheric properties can be constrained. However, if the radius and the mass of the planet are not known, as often is the case for non-transiting planets, atmospheric retrieval can

<sup>6</sup>A more detailed description of transmission spectroscopy is given in section 1.3.



lead to degeneracies as the shape of the spectral features depends on gravity. Thus, several different models can be retrieved from a single observed spectrum.

Detections of H<sub>2</sub>O on  $\beta$  Pictoris b (Chilcote, et al., 2017) at Gemini South, CO on HR 8799c (Konopacky, et al., 2013) with Keck Telescope and CH<sub>4</sub> on GJ 504 (Janson, et al., 2013) with Subaru have been reported with high confidence. Current high-contrast instruments capable of direct imaging are located on large-aperture telescope, e.g., Keck, GPI on Gemini, SCExAO on Subaru and SHERE on Very Large Telescope (VLT). Future space observatories such as *JWST*, *Roman Space Telescope*, and ground-based facilities, such as ELT, TMT, and GMT, will offer excellent sensitivity for direct imaging (Beichman, et al., 2019).

### 1.2.1 Composition of planetary atmospheres in our Solar system

Even before the first detection of exoatmospheres, we had indications that their composition will be very diverse. From the second half of the 20th century, we learned great detail about the composition of planetary atmospheres in our Solar system. These discoveries were possible due to several spacecrafts that studied the atmospheres directly.

Giant ice planets have retained their primary atmosphere and are mainly composed of hydrogen and helium. The inner planets have developed secondary atmospheres from internal volcanic activity and/or by an accumulation of material from comets. The Earth has developed a tertiary atmosphere which is produced by biological life.

Mercury has a very thin atmosphere that is constantly being renewed as its atoms are escaping into space due to low gravity and very high temperature that can reach up to 700 K on the surface. Traces of hydrogen, helium, sodium, potassium, calcium and oxygen have been found in Mercury's atmosphere (Bida, Killen & Morgan, 2000; Killen, et al., 2007). A very dense and hot atmosphere has been detected on Venus. It consists mostly of carbon dioxide and minor amount of nitrogen (Bertaux, et al., 2007).

Earth's atmosphere is dominated by molecular nitrogen and oxygen with traces of carbon dioxide, water, neon, and helium. Fig. 1.4 shows the Earth's transmission spectrum as measured by Pallé, et al. (2009) with the Nordic Optical Telescope and William Herschel Telescope from lunar eclipse observations. Transmission spectrum can be obtained by observing the light reflected from the Moon towards the Earth during the Lunar eclipse, which resembles the observing geometry during a planetary transit. As can be seen from Fig. 1.4, O<sub>2</sub> and H<sub>2</sub>O are the major atmospheric features in the spectrum. Other features are O<sub>3</sub>, N<sub>2</sub> and Ca II. These features, that are hindering spectra of stellar object observed from the Earth's surface, are called telluric lines. Thus, when observing exoplanets and other celestial objects from the ground, the signature of the Earth's atmosphere must be removed first (see sect. 3.4). The atmosphere of Mars consists mostly of carbon dioxide with some nitrogen and argon (Franz, et al., 2017). Methane was detected in the Mars' atmosphere (Formisano, et al., 2004) as well. Its origin was not yet fully explained and both geophysical and biogenic sources were proposed (Yung, et al., 2018).

Jupiter's atmosphere is mostly made of hydrogen and helium with traces of CH<sub>4</sub>, NH<sub>3</sub>, H<sub>2</sub>S, CO<sub>2</sub> and H<sub>2</sub>O. Montañés-Rodríguez, et al. (2015) performed transmission spectroscopy (see sect. 1.3) of Jupiter by observing its satellite Ganymed while it was passing through Jupiter's shadow. As Ganymed has practically no atmosphere (Broadfoot, et al.,

1981), it does not introduce any significant signal in the obtained spectrum. [Montañés-Rodríguez, et al. \(2015\)](#) detected CH<sub>4</sub> and H<sub>2</sub>O (Fig. 1.5) and reported absorption in the transmission spectra of Jupiter's atmosphere in the wavelengths corresponding to Na I in the upper atmosphere. Sodium presence in the upper atmosphere can possibly be explained by deposition of cometary impacts ([Noll, et al., 1995](#)). Saturn's atmosphere composition is similar to Jupiter's. Hydrogen and helium are the most abundant with traces of H<sub>2</sub>O and NH<sub>3</sub> ([Courtin, et al., 1983](#)). The atmosphere of Saturn is very dynamic as the winds can reach 1800 km/h ([Hueso, et al., 2020](#)). The Uranian atmosphere consists of hydrogen, helium, CH<sub>4</sub> and complex hydrocarbons e.g. ethane C<sub>2</sub>H<sub>6</sub> and acetylene C<sub>2</sub>H<sub>2</sub> that were produced from methane by photolysis ([Burgdorf, et al., 2006](#)). The Neptunian atmosphere is mostly made of hydrogen, helium, and traces of CH<sub>4</sub> ([Hubbard, 1997](#)). Winds in the atmosphere can reach 2100 km/h ([Suomi, Limaye & Johnson, 1991](#)).

To conclude, the planetary atmospheres in our Solar system are very diverse, however, they do not resemble the most studied exoatmospheres that belong to the hot gas giant planets. The most striking difference between hot-Jupiters and our Jupiter is their orbital distance. Hot Jupiters have their orbits within the orbit of Mercury. Such planets have temperatures usually between 1000 and 2000 K, with an extreme case of KELT-9b a planet found by [Gaudi, et al. \(2017\)](#) with temperature exceeding 4500 K. The large temperature of hot-Jupiters makes their atmospheres quite extended and easy to detect. We compare the scale heights  $H$  (see sect. 2 for a definition) of a hot-Jupiter WASP-76b and Jupiter. WASP-76b has a scale height of  $H=1212$  km, Jupiter has a scale height of  $H=27$  km. This makes the detection of any signature of Jupiters atmosphere very difficult and also explains why most of the atmospheric detections come from atmospheres of hot gas giants.

## 1.3 Transmission spectroscopy

As was already mentioned, the transmission spectroscopy technique can be used to characterize exoatmospheres of transiting exoplanets. During the transit, the light from the star passes through the exoatmosphere which leaves a small imprint on the light that can be detected (Fig. 1.6). The imprint is caused by additional absorption at certain wavelengths due to the presence of the planetary atmosphere. Spectroscopic time series covering the target before, during, and after transit are acquired to detect the planetary atmosphere. In other words, a transmission spectrum measures a thickness of the atmosphere as a function of wavelength. Spectrographs with very high stability (e.g. HARPS, ESPRESSO) are required to meet the necessary precision as careful treatment of the radial velocities is needed (see sect. 3.6). The obtained spectrum enables constraining the chemical composition and temperature-pressure profile as different chemical species are found in different atmospheric heights. Strong molecular bands like H<sub>2</sub>O, TiO, HCN and CO with strong absorption features can be found in extended exoatmospheres in the IR and/or visible. Atomic features of the alkali metals Na, K and Li have been detected only in the visible region (Table 1.1).

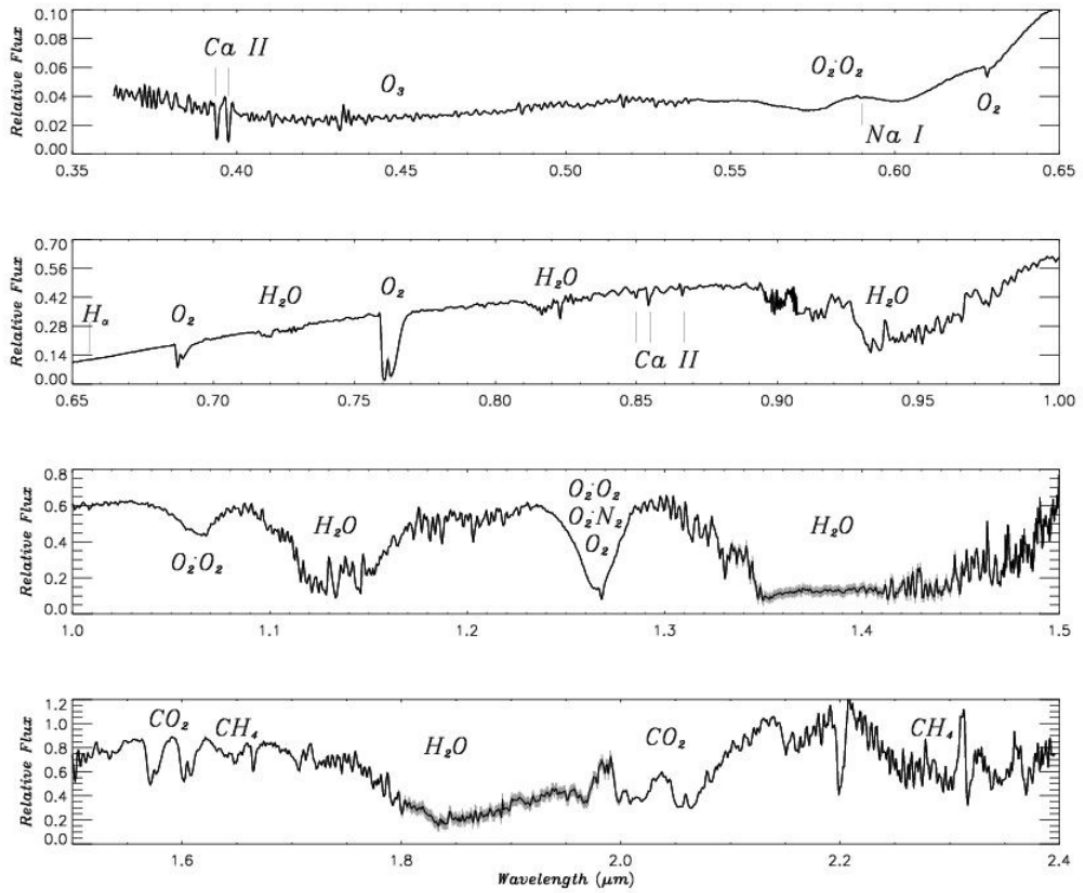


Figure 1.4: The Earth's transmission spectrum from 0.36 to 2.40  $\mu\text{m}$  (Pallé, et al., 2009).

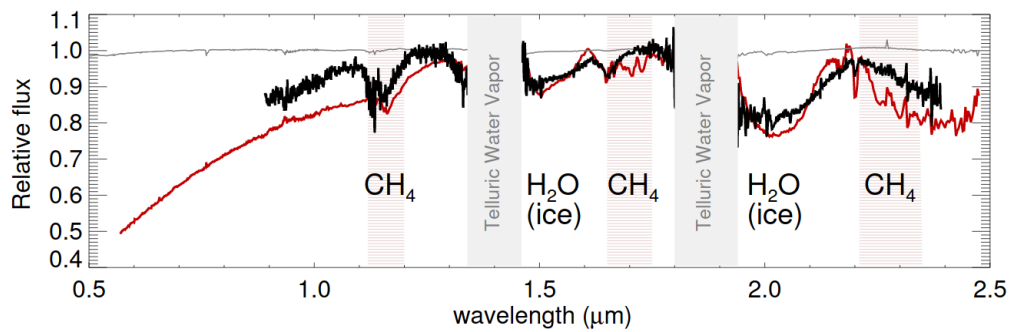


Figure 1.5: The transmission spectrum of Jupiter as measured with the WHT telescope (black) and VLT (red) (Montañés-Rodríguez, et al., 2015).

### 1.3.1 Low-resolution transmission spectroscopy

Low-resolution transmission spectroscopy is based on obtaining large number of spectra with spectrographs with low-resolving power  $R$ <sup>7</sup> ( $R < 8000$ ). The target and one or more

<sup>7</sup>The resolving power  $R$  is defined as the smallest wavelength difference  $\Delta\lambda$  between two spectral lines that can be distinguished at wavelength  $\lambda$  and can be written as:  $R = \frac{\lambda}{\Delta\lambda}$ .

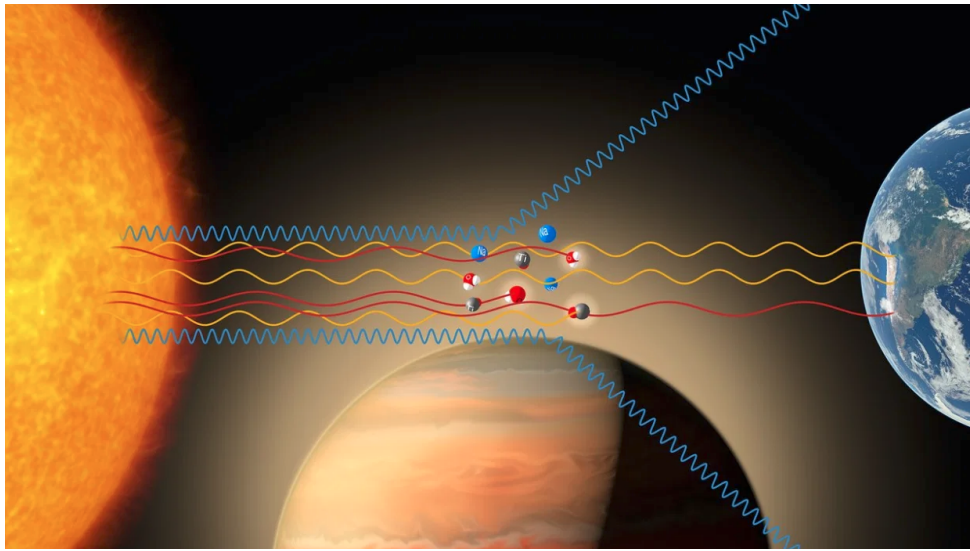


Figure 1.6: During a transit, light from the star passes through the planetary atmosphere which leaves a detectable imprint by creating an extra absorption due to the presence of the planetary atmosphere. Image credit: ESO/M. Kornmesser.

reference stars are observed and subsequently chromatic (color dependent) light curves are produced (Fig. 1.7) by binning the flux of the spectra in different regions. By studying the dependence of the transit depth on the wavelength, we can investigate which absorbers are present in the atmosphere.

Due to the availability of the low-resolution spectroscopy from space, early studies were done using only this technique (Charbonneau, et al., 2002; Vidal-Madjar, et al., 2003). *HST* and *Spitzer* are used for exoatmosphere characterization as the main advantage of space-based observations is that telluric features (caused by the presence of Earth's atmosphere) are not present in the observed spectrum. The *HST* has led to characterization of over 20 exoatmospheres. Ground-based instruments like FORS2 on the 8-m VLT (Sedaghati, et al., 2017), OSIRIS on the 10.4-m Gran Telescopio CANARIAS (GTC, Chen, et al., 2018), ACAM on the 4.2-m William Herschel Telescope (WHT, Kirk, et al., 2019) and IMACS on the 8.4-m Magellan Telescope (Espinoza, et al., 2019) were successfully used for exoatmospheres characterization.

The advantage of low-resolution transmission spectroscopy is that it uses low-resolving power  $R$ , thus is also suitable for fainter stars as with the same exposure time the  $SNR$  increases as the  $R$  decreases under the same conditions. Furthermore, several spectral regions can be covered with a single instrument. As an example, the FORS2 instrument can cover a wavelength region from 330 to 1100 nm<sup>8</sup>, thus, several spectral regions can be studied as can be seen in Fig. 1.8. Sedaghati, et al. (2017) detected TiO, Na, K in the atmosphere of WASP-19b. Low-resolution transmission spectroscopy is well suited to probe lower atmospheric heights compared to high-resolution spectroscopy (Fu, et al., 2017). While at low-resolution the transmission spectrum might appear entirely flat, narrow strong spectral

<sup>8</sup>Three separate grisms thus 3 transit nights are needed.

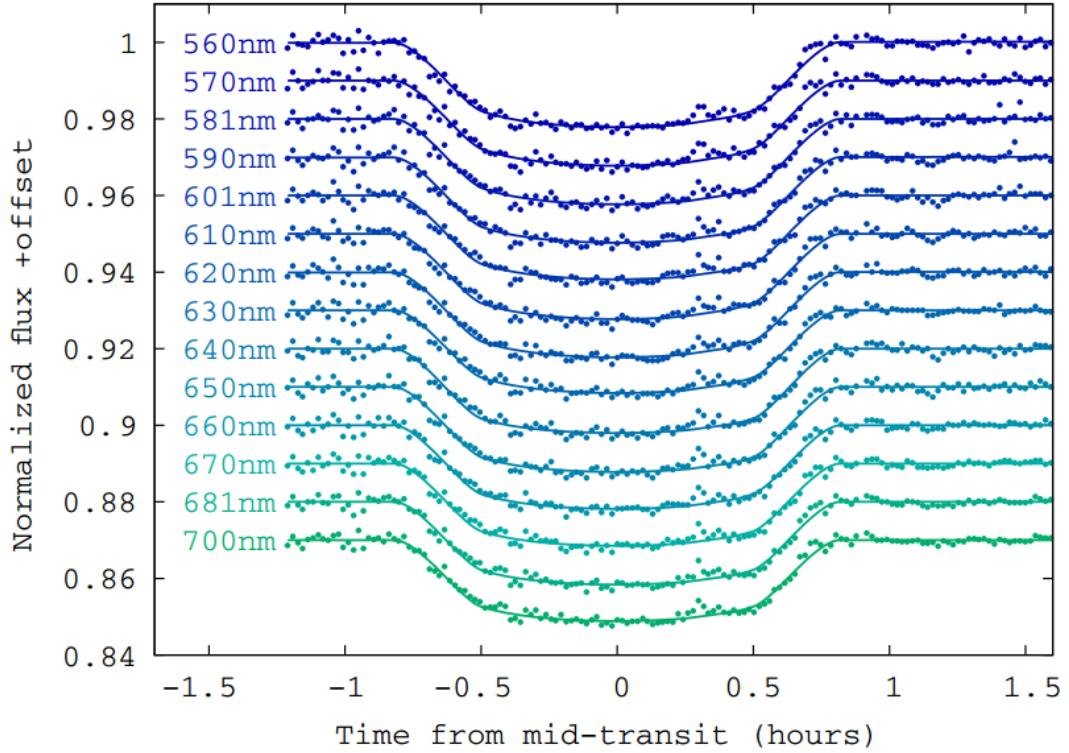


Figure 1.7: Band-integrated spectrophotometric light curves for the transit of WASP-19b. The central wavelength for each channel is indicated on the left-hand side of each plot. The integration width is mostly 20 nm. The modelled light curves for each channel are shown as solid lines (Boffin, et al., 2016).

lines should still remain optically thick above the cloud deck (Kempton, Perna & Heng, 2014). Disadvantages of the low-resolution transmission spectroscopy are that it requires a comparison standard star and it cannot spectrally resolve planetary features which can give more details about atmospheric composition (e.g. resolving sodium doublet) or planetary rotation (Snellen, et al., 2010).

### 1.3.2 High-resolution transmission spectroscopy

High-resolution transmission spectroscopy takes an advantage of high stability spectrographs with high resolving power  $R \gtrsim 50000$ . By comparing frames taken before and after transit to frames taken during transit, we can retrieve the planetary signal by removing the stellar signature. High-resolution transmission spectroscopy of exoatmospheres was firstly used from the ground by Snellen, et al. (2008) and Redfield, et al. (2008) as currently there are no high-resolution instruments available from space. This means that telluric features are always present and must be removed. A short overview of available methods for telluric correction is given in section 3.4. The high-resolution technique does not require standard



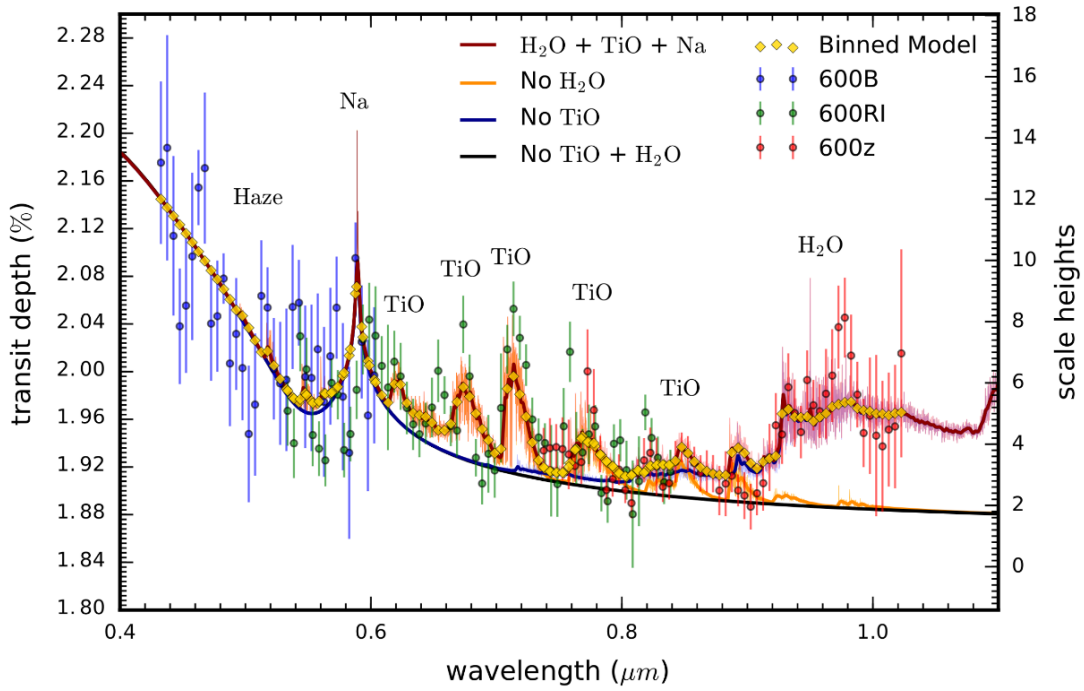


Figure 1.8: Atmosphere of WASP-19b as detected using the FORS2 instrument (Sedaghati, et al., 2017).

star however due to the demands on the very high resolving power, it is limited for bright objects (more light is needed for spectrographs with very high resolving power).

A very precise treatment of radial velocities is necessary in order to retrieve the planetary signal (sect. 3.5). Recent instruments, e.g. GIARPS (Claudi, et al., 2017) mounted at the 3.6m Telescopio Nazionale Galileo (TNG), have comparable wavelength coverage to the low-resolution instruments where the full wavelength coverage can be usually achieved with several transit nights. High-resolution transmission spectroscopy allows planetary features to be fully resolved, thus, allowing detail study of the planetary features including the atmosphere. From the resolved features, planetary rotation (by measuring rotational broadening), winds (by measuring Doppler effect) and chemical composition can be derived. Besides sodium detections, later studies added potassium (Keles, et al., 2019), helium (Nortmann, et al., 2018), scandium (Astudillo-Defru & Rojo, 2013) and hydrogen that can be used to study atmospheric escape (Yan & Henning, 2018). For molecular detection, it is more favorable to use the cross-correlation function (CCF) method (Hoeijmakers, et al., 2018) as the molecular lines are composed of many weak individual lines. The CCF method takes advantage of the very high resolution, and the final spectra are cross-correlated with a planetary template containing the expected molecules. This method was successfully used to detect H<sub>2</sub>O (Birkby, et al., 2013), TiO (Nugroho, et al., 2017), HCN (Hawker, et al., 2018) and CO (Snellen, et al., 2010) as well as atomic species Fe, Ti (Hoeijmakers, et al., 2019).

### 1.3.3 High-resolution spectrographs

High-resolution spectroscopy relies on very high resolving power which can be achieved using echelle spectrographs. Echelle spectrograph disperses the light in two perpendicular directions using a cross-disperser together with a grating. The results can be detected as a 2D pattern on a CCD camera chip. The main property of every spectrograph is its resolving power  $R$ . Besides the actual scientific frame, a set of calibration frames is usually taken. This set includes flat-field frames, bias frames, and frames with a comparison spectrum produced by a lamp<sup>9</sup> with well-defined composition (Thorium cathode in Argon atmosphere (thus called ThAr lamp) is widely used for high-resolution spectroscopy in the optical region) producing spectral lines that can be used for the wavelength calibration.

Echelle spectrographs are often used for measurements of radial velocities as they offer greater wavelength range (and more spectral lines for the cross-correlation function) for given resolution compared to a single slit spectrograph. To obtain the radial velocity measurement, cross-correlation function can be used. It is a measurement of the similarity of two series as a function of the displacement of one relative to the other. The current spectrographs can achieve very high precision by using very high resolving power ( $R \geq 10^5$ ) and/or having a large wavelength coverage. Modern high-resolution echelle spectrographs mounted at large telescopes are: HIRES at 10-m Keck Telescope (Vogt, et al., 1994), MIKE at 6.5-m Magellan telescope (Bernstein, et al., 2003), HDS at 8.2-m Subaru Telescope (Noguchi, et al., 2002), UVES at 8.2-m VLT (Dekker, et al., 2000), HRS at the 9.2-m Hobby Eberly Telescope (Tull, 1998) and PEPSI at the Large Binocular Telescope (2x8.4-m, Strassmeier, et al., 2015). In the text below, we provide more details about two high-resolution spectrographs most relevant for exoatmosphere characterization in this thesis (HARPS and ESPRESSO).

#### HARPS

The High Accuracy Radial Velocity Planet Searcher (HARPS, Mayor, et al., 2003) is a temperature- and pressure-controlled fiber-fed echelle spectrograph (see Fig. 1.9) mounted on the 3.6-m telescope at the La Silla observatory in Chile. It was installed in 2002 and acquired first light in 2003. It is currently operated by the European Southern Observatory (ESO). Its stability makes it an ideal instrument for the measurement of radial velocities of exoplanets as it can achieve long term radial velocity accuracy on the order of  $1 \text{ m s}^{-1}$  for late-type slowly-rotating stars.

The spectrograph has contributed to the discovery of more than 150 exoplanets. HARPS is fed by two 70-micron fibers corresponding to 1 arcsecond on the sky. The spectrum has 68 spectral orders and is recorded by 2 CCDs. During observations, one of the fibers is collecting light from the star. The second fiber can be either used to simultaneously obtain a Thorium-Argon reference spectrum or the background sky. The Th-Ar lamp is located in a separate calibration unit and is connected to the telescope focus via fibre link. Both spectra (star and Th-Ar) are recorded simultaneously by the CCD in one exposure. HARPS has a wavelength coverage from 380 to 690 nm. The resolving power is  $R = 115\,000$ . An example of a raw frame is shown in Fig 1.10 where echelle orders are apparent.

<sup>9</sup>A gas cell (e.g. an iodine absorption cell) can also be used for the wavelength calibration (Hatzes & Cochran, 1992).

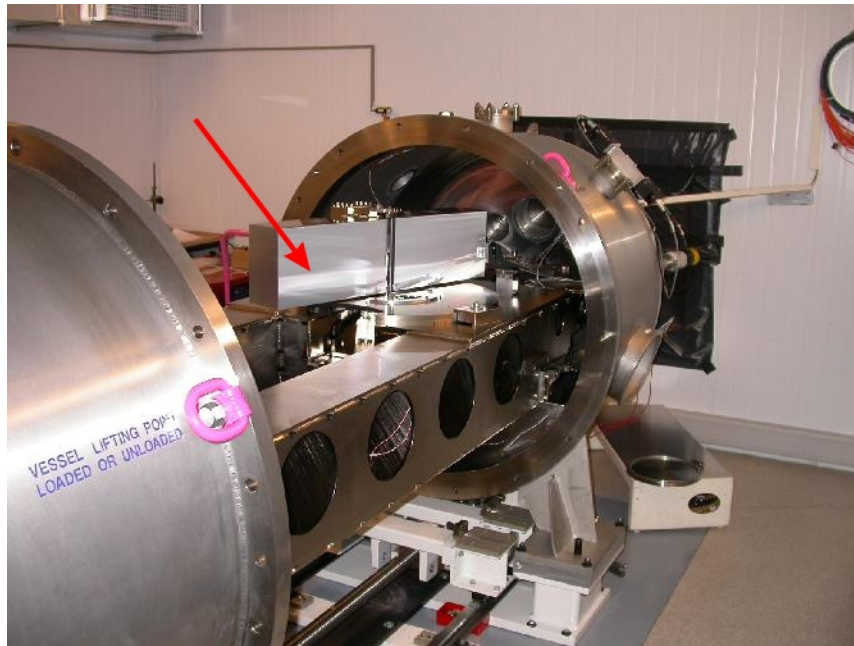


Figure 1.9: Side view of the HARPS. The grating of the echelle is visible and highlighted with the red arrow. Source: ESO.

Furthermore, its stability, accuracy and high resolving power make it an ideal instrument for characterization of exoatmospheres. Since [Wytttenbach, et al. \(2015\)](#) used it for the first time, HARPS was used for several exoatmospheric studies of bright targets since 3.6-m collecting aperture limits its usage only to bright targets ([Wytttenbach, et al., 2017](#); [Seidel, et al., 2019](#); [Žák, et al., 2019](#)). HARPS will be supplemented by the Near Infra-Red Planet Searcher (NIRPS) instrument in late 2020 ([Bouchy, et al., 2019](#)). It will be possible to use both instruments simultaneously to obtain coverage in the optical and NIR. The success of HARPS led to a similar spectrograph called HARPS-N that is mounted at the 3.6-m Telescopio Nazionale Galileo at Roque de los Muchachos Observatory at La Palma in Spain. Furthermore, HARPS3 is planned for the 2.54-m Isaac Newton Telescope in the near future ([Thompson, et al., 2016](#)).

## ESPRESSO

The new instrument placed at Paranal in Chile called Echelle SPectrograph for Rocky Exoplanets and Stable Spectroscopic Observations (ESPRESSO, [Pepe, et al., 2014](#); [González Hernández, et al., 2018](#)) is an ultra-stable spectrograph installed at the VLT. It is a high-resolution fibre-fed echelle spectrograph. It can either be operated in configuration with 1 unit (1-UT) or 4 units (4-UT) of the VLT (there are four 8-m telescopes located at the VLT facility). Each configuration has its own characteristics; in 1-UT configuration it has a resolving power of  $R = 140\,000$  or  $R = 190\,000$  and can reach limiting V-band magnitude of 17 and 16 respectively<sup>10</sup>. In 4-UT configuration it can operate with resolving power  $R = 70\,000$  and reach limiting magnitude of 20. The spectrograph is fed by

<sup>10</sup>Based on an approximate S/N per binned pixel of 10 in one hour.



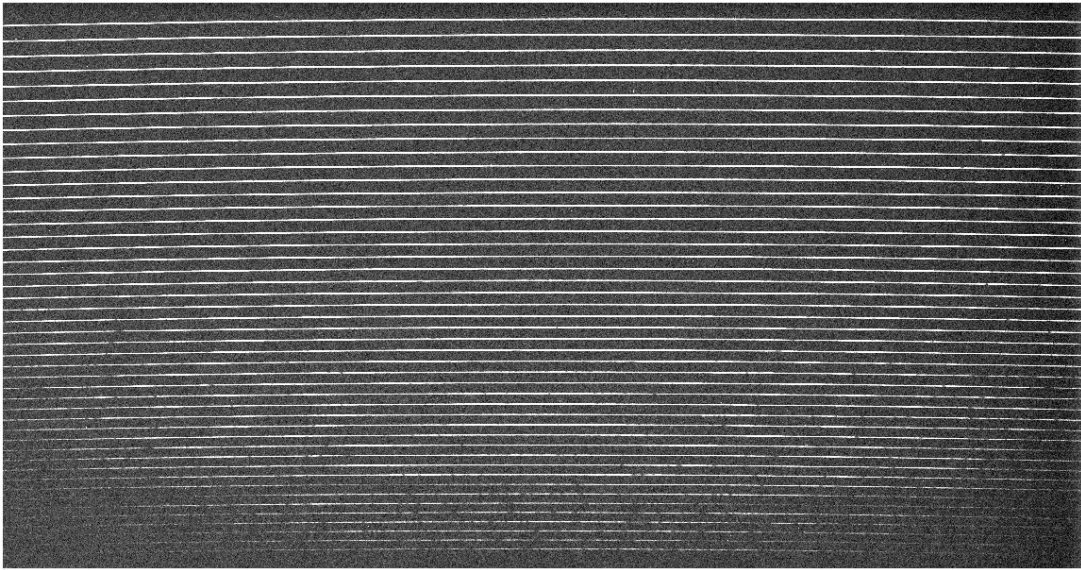


Figure 1.10: Raw frame of WASP-166b from HARPS. Source: ESO archive.

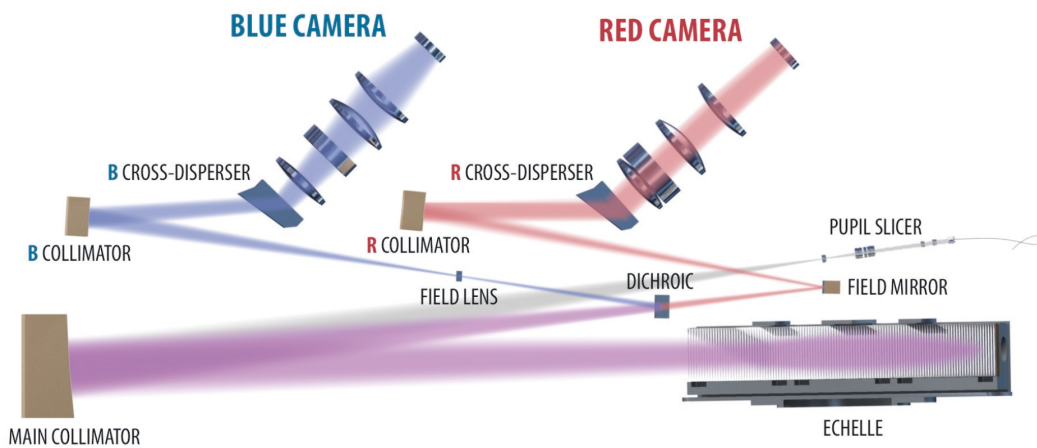


Figure 1.11: Schematics of the ESPRESSO instrument. Light goes from the telescope to the echelle grating and the final image is recorded by two CCD cameras. Source: ESO.

two fibres, one is used for the target while the second one can be used for simultaneous calibration (either the sky or simultaneous reference). The image is recorded by two CCD cameras optimized for the blue and red regions (see Fig. 1.11). The wavelength coverage is from 380 to 788 nm providing several important regions not accessible with HARPS. Furthermore, the ESPRESSO has a coverage of the 740 nm H<sub>2</sub>O band and 766.5/769.9 nm potassium lines. Despite being installed in 2018, ESPRESSO has already delivered first scientific results on exoatmospheres. [Ehrenreich, et al. \(2020\)](#) detected iron on the day-side of WASP-76b and [Chen, et al. \(2020\)](#) has reported the presence of sodium, neutral hydrogen, and potassium in the atmosphere of WASP-52b.

## Chapter 2

# Exoatmosphere detectability and target selection

A large number of known planets greatly exceeds the capability of available observing time. Current ground-based telescopes are not able to provide enough observing time to perform follow up of all exoplanets. Thus to maximize gained information, we have established a guideline for selecting the best targets for transmission spectroscopy observations ([Kabáth, et al., 2019](#)).

The atmosphere can be defined with a scale height  $H$  which, represents the vertical distance by which the pressure is reduced by a factor of  $e$ , is defined as:

$$H = \frac{T_p k_B}{g \mu_m}, \quad (2.1)$$

In eq. 2.1,  $k_B$  is the Boltzmann constant,  $T_p$  is the temperature of the planetary atmosphere,  $\mu_m$  is the mean molecular weight and  $g$  is the planet surface gravity ( $g = \frac{GM_p}{R_p^2}$ , where  $G$  is the gravitational constant;  $M_p$  and  $R_p$  are the mass and the radius of the planet). The larger the value of  $H$ , the more extended is the atmosphere of a certain planet.

If the atmosphere is not very extended, it might be difficult to detect atmospheric features with confidence. The magnitude of the transmission spectra signal (an increase of transit depth due to the exoplanetary atmosphere, [Seager, Deming & Valenti, 2009](#))  $\Delta\delta$  can be estimated as :

$$\Delta\delta \simeq \frac{2n_\lambda H R_p}{R_s^2}, \quad (2.2)$$

where  $R_s$  is the stellar radius and  $n_\lambda$  is the number of the atmospheric scale heights at certain wavelength ([Deming, Louie & Sheets, 2019](#)). As an illustration,  $\Delta\delta \simeq 6 \cdot 10^{-5}$  for WASP-18b, a planet with large surface gravity (bad target for transmission spectroscopy); while  $\Delta\delta \simeq 3 \cdot 10^{-3}$  for WASP-127b, a planet with an extended atmosphere (good target for transmission spectroscopy).

The situation in detecting exoatmospheres is further complicated by many factors. First, both stellar and planetary spectra are shifted from each other due to the doppler effect caused by the planetary orbital motion as the planet is orbiting the star and each taken spectrum thus must be individually corrected for it. Thus, radial velocity corrections

of stellar and planetary spectra are needed and the stability of the used spectrograph must be considered since the radial velocities can be in the order of m/s. It is more difficult to obtain precise radial velocities for an A-type star rather than for G-type star due to the fewer number of spectral lines and higher rotational velocities of early type stars. The inability to obtain precise radial velocities in early type star might hinder our ability to retrieve the planetary signal. At last, transit duration must also be taken into account. If the transit is too short, it will be difficult to obtain enough in-transit frames.

## 2.1 Target selection

We followed the guidelines of the previous section for the target selection (brightness of the star, temperature and gravity of the planet, spectral type of the star). We searched the ESO archive and found 4 suitable hot inflated gas giant planets with archival data from the HARPS instrument. The selection of the targets was based on their large transmission signal  $\Delta\delta$  (Fig. 2.1), the number of transit nights available, the *SNR* (signal to noise ratio) of the spectra and that the data were not previously published. We present a description of the selected planets in the following subsections.

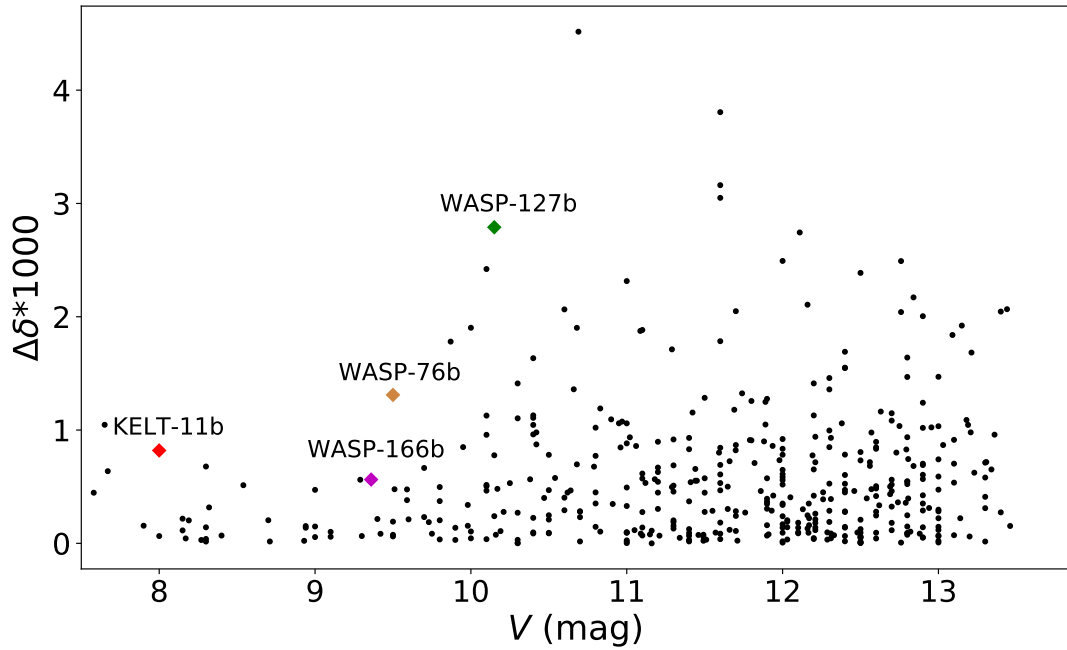


Figure 2.1: Transmission signal  $\Delta\delta$  versus visual magnitude  $V$  of the host stars of the known exoplanets with measured mass. The candidates available in archive selected for the investigation are plotted in color. Data are from exoplanet.eu database (Schneider, et al., 2011).

### 2.1.1 WASP-76b

WASP-76b is an ultra-hot Jupiter with short orbital period of  $P = 1.81$  days, mass of  $M_p = 0.92 M_{\text{Jup}}$  and radius of  $R_p = 1.83 R_{\text{Jup}}$  discovered by [West, et al. \(2016\)](#). The extended atmosphere with scale height of  $H = 1212$  km and high temperature of  $T_p = 2190$  K make it one of the best targets for transmission spectroscopy ([Kab  th, et al., 2019](#)). WASP-76b is the only ultra-hot Jupiter in our sample. Ultra-hot Jupiters can exhibit thermal inversions in the atmospheres which can be caused by TiO and/or VO. See section 4.1 for discussion of new papers after initial submission of our manuscript ([    k, et al., 2019](#)). System parameters are listed in table 2.1.

### 2.1.2 WASP-127b

WASP-127b is a hot bloated super-Neptune with orbital period of  $P = 4.18$  days, mass of  $M_p = 0.18 M_{\text{Jup}}$  and radius of  $R_p = 1.37 R_{\text{Jup}}$  discovered by [Lam, et al. \(2017\)](#). Its extended atmosphere with a scale height of  $H = 2500$  km makes it another good target for transmission spectroscopy. System parameters are listed in table 2.1. This planet was initially studied by [Palle, et al. \(2017\)](#) using the 2.5-m Nordic optical telescope (NOT) who reported a cloud-free atmosphere. Subsequently, it was studied by [Chen, et al. \(2018\)](#) who detected the presence of sodium, potassium, and lithium in the optical and H<sub>2</sub>O in the near-infrared (Fig. 2.2) using the OSIRIS at GTC. See section 4.2 for further discussion.

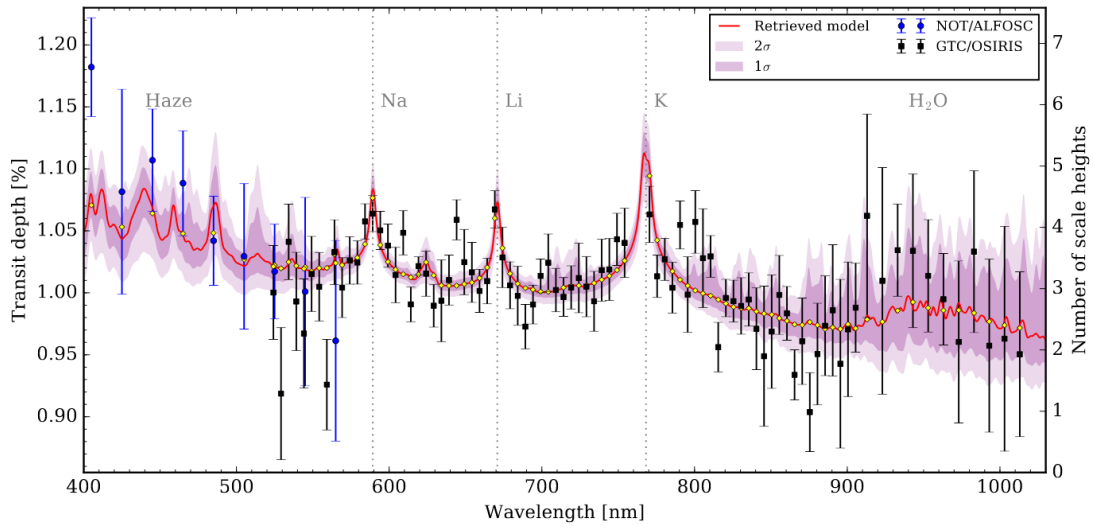


Figure 2.2: Atmosphere of WASP-127b as detected by GTC ([Chen, et al., 2018](#)).

### 2.1.3 KELT-11b

KELT-11b is a hot inflated planet with orbital period of  $P = 5.44$  days, mass of  $M_p = 0.10 M_{\text{Jup}}$  and radius of  $R_p = 0.63 R_{\text{Jup}}$  discovered by [Pepper, et al. \(2017\)](#). Due to its

extended atmosphere and large scale height  $H = 2763$  km, it was suggested as an ideal target for transmission spectroscopy (Kab  th, et al., 2019). System parameters are listed in Table 2.1.

### 2.1.4 WASP-166b

WASP-166b is a hot inflated Neptune with orbital period of  $P = 4.74$  days, mass of  $M_p = 0.195 M_{Jup}$  and radius of  $R_p = 1.37 R_{Jup}$  discovered by Hellier, et al. (2019). With a scale height of  $H = 1103$  km, it is an excellent target to investigate atmospheres of hot Neptunes. System parameters are listed in table 2.1.

Table 2.1: Properties of the four targets (star and planet) considered in this thesis.

	Parameters	WASP-76	WASP-127
Star	$V$ (mag)	9.5	10.5
	Sp. Type	F7	G5
	$M_s$ ( $M_\odot$ )	$1.46 \pm 0.07$	$1.31 \pm 0.05$
	$R_s$ ( $R_\odot$ )	$1.73 \pm 0.04$	$1.33 \pm 0.03$
	$T_{eff}$ (K)	$6250 \pm 100$	$5750 \pm 100$
	$\log g$	$4.4 \pm 0.1$	$3.9 \pm 0.1$
Planet	$M_p$ ( $M_{Jup}$ )	$0.92 \pm 0.03$	$0.18 \pm 0.02$
	$R_p$ ( $M_{Jup}$ )	$1.83^{+0.06}_{-0.04}$	$1.37 \pm 0.04$
	Period (d)	$1.809886 \pm 0.000001$	$4.178062 \pm 0.000002$
	Transit duration (days)	$0.1539 \pm 0.0008$	$0.1795 \pm 0.0007$
	Orbital Semi-major axis (AU)	$0.33 \pm 0.0005$	$0.052 \pm 0.0005$
	Orbital inclination (degrees)	$88.0^{+1.3}_{-1.6}$	$88.7^{+0.8}_{-0.6}$
	Reference	West, et al. (2016)	Lam, et al. (2017)
	Parameters	WASP-166	KELT-11
Star	$V$ (mag)	9	8
	Sp. Type	F9	G8/K0
	$M_s$ ( $M_\odot$ )	$1.19 \pm 0.06$	$1.438^{+0.061}_{-0.052}$
	$R_s$ ( $R_\odot$ )	$1.22 \pm 0.06$	$2.72^{+0.21}_{-0.17}$
	$T_{eff}$ (K)	$6050 \pm 50$	$5370^{+51}_{-50}$
	$\log g$	$4.5 \pm 0.1$	$3.727^{+0.04}_{-0.046}$
Planet	$M_p$ ( $M_{Jup}$ )	$0.102 \pm 0.004$	$0.195^{+0.019}_{-0.018}$
	$R_p$ ( $M_{Jup}$ )	$0.63 \pm 0.03$	$1.37^{+0.15}_{-0.12}$
	Period (d)	$5.443526 \pm 0.00001$	$4.736529^{+0.000068}_{-0.000059}$
	Transit duration (days)	$0.148 \pm 0.008$	$0.3051^{+0.0053}_{-0.0051}$
	Orbital Semi-major axis (AU)	$0.0642 \pm 0.0001$	$0.06229^{+0.00088}_{-0.00076}$
	Orbital inclination (degrees)	$87.8 \pm 0.6$	$85.8^{+2.4}_{-1.8}$
	Reference	Hellier, et al. (2019)	Pepper, et al. (2017)

# Chapter 3

## Data sets and Analysis

### 3.1 Data sets

Table 3.1 shows the various datasets we used. For illustration purposes, we show part of the spectrum around the sodium Na D region of each of our targets, along with the telluric spectrum and spectrum after telluric correction in Fig. 3.1.

#### **WASP-76b:**

The HARPS data are covering 3 transit events, on 11/12 November 2012, 24/25 October 2017 and 22/23 November 2017. The total number of frames was 176 with 105 in-transit, and the exposure times were between 300-600 seconds.

#### **WASP-127b:**

The HARPS data are covering 2 transit events during the nights of 27/28 February and 19/20 March 2017. The total number of frames was 82, of which 52 were in-transit.

#### **WASP-166b:**

The HARPS data are covering three transits during the nights of 13/14 January, 03/04 March and 14/15 March 2017. The total number of frames was 188, of which 112 were in-transit.

#### **KELT-11b:**

The HARPS data are covering 3 transit events and 4 nights of out-of-transit on 01/02 February (transit), 14/15 February, 15/16 February (transit), 16/17 February, 05/06 March, 06/07 March (transit) and 07/08 March 2017. The total number of frames was 342, of which 144 were in-transit.

### 3.2 Data reduction

We retrieved the publicly available HARPS (Mayor, et al., 2003) reduced spectroscopic data sets from the ESO Science data archive for the four planets WASP-76b, WASP-127b,

Table 3.1: Observing logs for all four data sets. Number in parenthesis represents number of frames taken in-transit. Median  $SNR$  is derived across all the orders. The last column states  $SNR$  from the 16th order (585.03-591.62 nm) of the echelle spectrum, corresponding to the position of the sodium doublet line.

Date	No. Spectra	Exp. Time [s]	Airmass range	Median $SNR$	$SNR^{16}$
WASP-76					
2012-11-12	64 (40)	300	1.79-1.18-1.48	21.1-31.6	13.3-20.6
2017-10-25	49 (27)	400-600	1.75-1.18-2.10	32.1-55.8	18.7-34.2
2017-11-23	66 (40)	300-400	1.42-1.18-2.45	30.7-53.5	15.5-31.8
WASP-127					
2017-02-28	37 (22)	500	1.40-1.11-1.47	29.9-40.0	14.7-20.1
2017-03-20	45 (30)	500-600	1.98-1.11-1.55	26.4-38.2	14.0-19.5
WASP-166					
2017-01-14	75 (39)	300-350	2.37-1.01-1.17	20.0-52.8	11.0-33.0
2017-03-04	52 (39)	300-400	1.01-1.21-2.55	26.4-65.0	13.5-37.3
2017-03-15	66 (34)	350	1.17-1.01-2.35	18.8-55.3	8.6-29.9
KELT-11					
2017-02-02	37 (24)	300	1.42-1.11-1.08	81.2-92.8	45.6-53.4
2017-02-15	28 (0)	400	1.11-1.08-1.25	85.4-106.8	45.4-59.2
2017-02-16	69 (49)	400	2.29-1.06-1.93	46.1-115.3	24.9-64.8
2017-02-17	27 (0)	400	1.81-1.23-1.07	67.5-95.4	39.0-55.5
2017-03-06	42 (0)	300	1.06-1.21-2.04	26.3-89.6	11.1-43.4
2017-03-07	93 (71)	300	2.23-1.06-2.41	48.6-83.1	26.1-45.5
2017-03-08	46 (0)	300	1.60-1.12-1.09	70.1-91.3	38.4-50.2



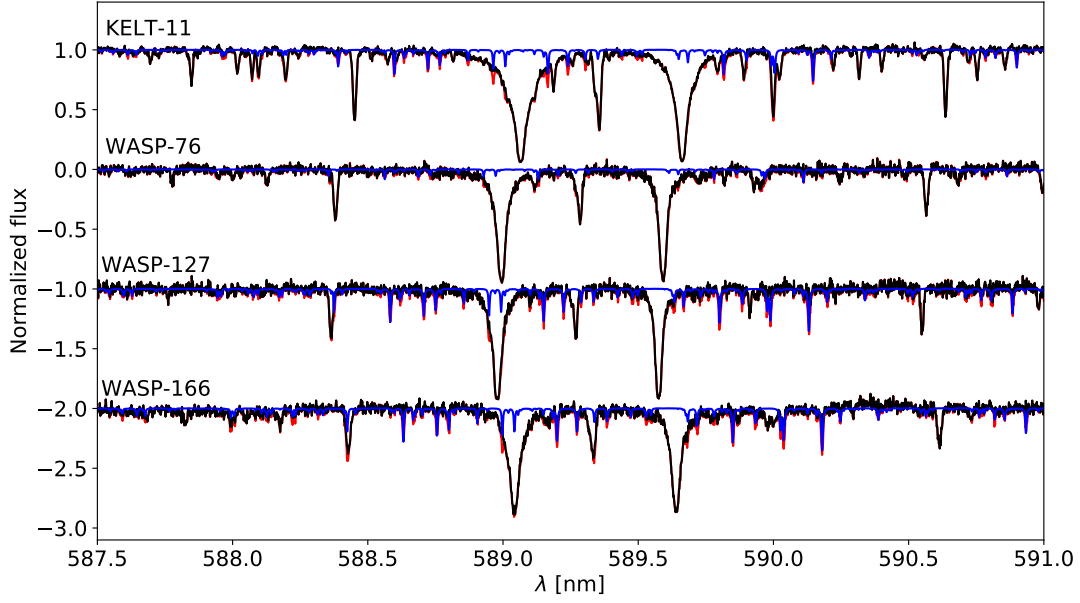


Figure 3.1: Illustration of the spectral region around the Na D lines for one selected example spectrum for each of our targets. The observed spectra in red are presented in the stellar reference frame during mid-transit. Telluric spectra are shown in blue. Observed spectra after telluric correction are presented in black (Žák, et al., 2019).

WASP-166b, and KELT-11b (see Table 3.1). Data were obtained under program IDs 090.C-0540(F), 098.C-0304(A), and 0100.C-0750(A). The retrieved data are fully reduced products obtained with the HARPS Data Reduction Software (DRS version 3.5). In more detail, each spectrum is provided as a merged 1D spectrum with 0.001 nm wavelength step. The reduced spectrum covers the wavelength range between 380 nm and 690 nm, and has a resolving power  $R \approx 115\,000$  corresponding to  $2.7\text{ km s}^{-1}$  per resolving element. Spectra are already corrected to the Solar system barycentric frame of reference. The sodium doublet is well-centered on the 16th order of HARPS (see Fig. 3.1). In the next subsections we will perform the following steps: normalization of the flux  $\rightarrow$  correction of stellar radial velocities  $\rightarrow$  telluric correction  $\rightarrow$  correction of radial velocities to retrieve the planetary signal  $\rightarrow$  obtain final transmission spectrum.

### 3.3 Normalization

We obtained the radial velocities<sup>1</sup> of the star from the FITS header of the spectra and subsequently shifted both during transit  $f(\lambda, t_{\text{in}})$  and out of transit  $f(\lambda, t_{\text{out}})$  frames to the stellar frame during mid-transit (zero orbital radial velocity). We have made a cut of the region of interest and performed flux normalization for the obtained spectra  $f(\lambda, t_{\text{in}}) \rightarrow \tilde{f}(\lambda, t_{\text{in}})$  and  $f(\lambda, t_{\text{out}}) \rightarrow \tilde{f}(\lambda, t_{\text{out}})$ , where the tilde represents normalization. Normalization has been carried out using the standard IRAF (Tody, 1986) task continuum. More precisely, a Legendre polynomial has been used to perform the normalization of continuum regions

<sup>1</sup>Radial velocity of the star caused by its motion in space with respect to the Solar barycenter



without strong lines within the regions centered around the Na D lines (583–596 nm), H $\alpha$  (645–670 nm), H $\beta$  (475–495 nm), and lithium (666–674 nm).

### 3.4 Telluric correction

Ground-based observations suffer from the telluric contamination which can be very prominent especially in the IR region, however, it is also present in the optical. The origin is the presence of the Earth’s atmosphere that is causing absorption features. Example of the telluric spectra is shown in Fig. 1.4. There are several ways of removing the signature of Earth’s atmosphere. One can use a standard star to subtract the telluric spectrum. Standard star is usually a rapidly rotating early-type star (their spectrum is relatively featureless) located near the target on the sky. The narrow telluric lines can be easily distinguished from the rotation-broaden stellar lines. However, this approach is very limiting by the number of suitable standard stars and also it increases the observing time. The approach by [Chen, et al. \(2020\)](#) uses *Molecfit* software to remove telluric features. *Molecfit* is a software tool to correct astronomical observations for atmospheric absorption features, based on fitting synthetic transmission spectra to the astronomical data. It can also estimate molecular abundances, especially the water vapour content of the Earth’s atmosphere ([Smette, et al., 2015](#)). Another approach was used by [Casasayas-Barris, et al. \(2017\)](#) that fits synthetic telluric spectrum to the observed one.

Since we had scaling issues with *Molecfit* we decided to follow the method outlined in [Casasayas-Barris, et al. \(2017\)](#). We took the 1D telluric spectrum constructed from the line list of HITRAN ([Rothman, et al., 2013](#)) and scaled its resolution to match the resolution of our spectra. Then we corrected the reference telluric spectrum for the radial velocity to the same frame as the observed spectrum. The telluric line’s absorption depth is changing with the airmass. Thus, we used a least-squares method on the unblended telluric lines to scale the telluric model to the same airmass (depth) as the observed spectrum. Afterwards, we divided each observed spectrum by the telluric spectrum scaled for the given airmass using standard IRAF commands resulting in the removal of the telluric lines.

As discussed in [Casasayas-Barris, et al. \(2017\)](#), the scaling of the telluric spectra is not perfect as line depth variation is not equal for all the telluric lines, hence possibly introducing small residuals into the final transmission spectrum. As an illustration of the goodness of the telluric lines removal, the root mean square (RMS) of a single-night transmission spectrum in the telluric region (589.9–590.4 nm) before applying the telluric correction is 0.00339, the RMS of the same region was decreased to 0.00196 after applying the correction. For comparison, the RMS of the spectral region without telluric features (587–587.5 nm) is 0.00193.

### 3.5 Rossiter-McLaughlin effect

The Rossiter-McLaughlin (RM) effect is a spectroscopic phenomenon when an object is moving across the disc of a star. The RM effect was early observed in eclipsing binary systems ([Rossiter, 1924](#); [McLaughlin, 1924](#)), nowadays it is also studied for transiting exoplanets ([Queloz, et al., 2000](#); [Addison, et al., 2016](#)).

Due to the rotation of a star, half of the visible surface of the star is moving towards the observer and the second half is moving away. During transit, an object will obscure part of the visible surface of the star, thus, we will be temporarily detecting more photons (and stellar spectral lines) that are either red- or blue-shifted (Fig. 3.2). After the object moves to the other side of the disc, the effect will be the opposite. We can estimate the RM effect amplitude with the following formula (Triaud, 2018):

$$\Delta v_r \simeq \frac{2}{3} \left( \frac{R_p}{R_s} \right)^2 V \sin i \sqrt{1 - b^2}, \quad (3.1)$$

where  $V \sin i$  is the projected rotational velocity of the star,  $b$  is the impact parameter<sup>2</sup>. Using the equation 3.1, we can estimate the RM amplitude values:  $2.3 \text{ ms}^{-1}$  for WASP-76b,  $2 \text{ ms}^{-1}$  for WASP-127b,  $8 \text{ ms}^{-1}$  for WASP-166b and  $4 \text{ ms}^{-1}$  for KELT-11b.

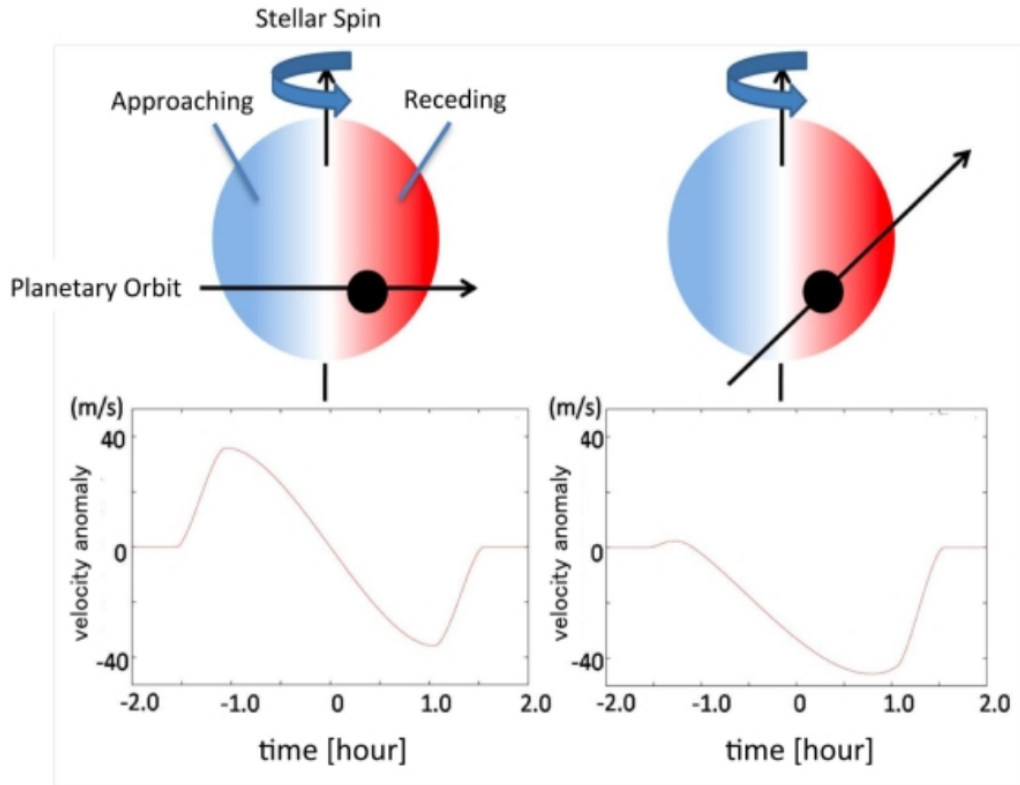


Figure 3.2: Schematic of the Rossiter-McLaughlin effect. During transit, when the planet blocks the approaching side of the star (blue), the radial velocity shows an apparent red-shift. Left image shows alignment between the stellar spin axis and the planetary orbit axis. Right panel shows misalignment of the two axes by 50 degrees. Image credit: subarutelescope.org.

<sup>2</sup>The impact parameter  $b$  is defined geometrically as the relative projected distance between the planet and star centres during mid-transit.

### 3.6 Transmission spectrum

After the telluric correction, we averaged all the out-of-transit spectra shifted to a stellar reference frame during mid-transit to create a “master out” frame  $\tilde{F}_{\text{out}}(\lambda) = \sum_{\text{out}} \tilde{f}_{\text{out}}(\lambda, t_{\text{out}})$ . Next, we divided each in-transit frame  $\tilde{f}_{\text{in}}(\lambda, t_{\text{in}})$  by  $\tilde{F}_{\text{out}}(\lambda)$  to create the individual transmission spectra. Each of these frames was subsequently corrected for the planetary motion as the planetary signal is shifted from the stellar reference frame by  $v_p$  which is defined as:

$$v_p(\phi) = K_p \sin(2\pi\phi), \quad (3.2)$$

where  $K_p = K_s \frac{M_p}{M_s}$  is the radial velocity semi-amplitude of the planet,  $\phi$  is the orbital phase of the planet in respect to the transit midpoint and  $K_s$  is the radial velocity semi-amplitude of the star.

This approach was presented by [Wytttenbach, et al. \(2015\)](#) and allows better retrieval of the atmospheric features compared to the approach used by [Redfield, et al. \(2008\)](#) which does not account for the planetary motion, thus the planetary signal cannot be fully retrieved. We created a model of radial velocity of the planet taking only out-of-transit data as the in-transit data are affected by the RM effect. The planetary signal is shifted by as much as tens of kilometers per second from the transit midpoint. The usage of the raw observed radial velocities would imply correcting for the possible Rossiter-McLaughlin effect and would produce systematic effects in the final transmission spectrum ([Cegla, et al., 2017](#); [Wytttenbach, et al., 2017](#)). Finally, we summed up all the individual transmission spectra and normalized this sum to unity and then subtracted unity to retrieve the final transmission spectrum,  $\tilde{\mathcal{R}}(\lambda)$ :

$$\tilde{\mathcal{R}}(\lambda) = \sum_{\text{in}} \frac{\tilde{f}_{\text{in}}(\lambda, t_{\text{in}})}{\tilde{F}_{\text{out}}(\lambda)} \Big|_{\text{Planet RV shift}} - 1 \quad (3.3)$$

### 3.7 Stellar activity

As stellar activity can resemble or cancel out planetary signals it is important to monitor it during observations. One approach is to use specific lines that are sensitive to the stellar activity. Calcium and magnesium lines were used by [Wytttenbach, et al. \(2017\)](#) and [Chen, et al. \(2020\)](#). We have used the same method and results can be seen in Fig. 3.3. Featureless spectra imply that the effects of the stellar activity are negligible and will not hinder our planetary signals.

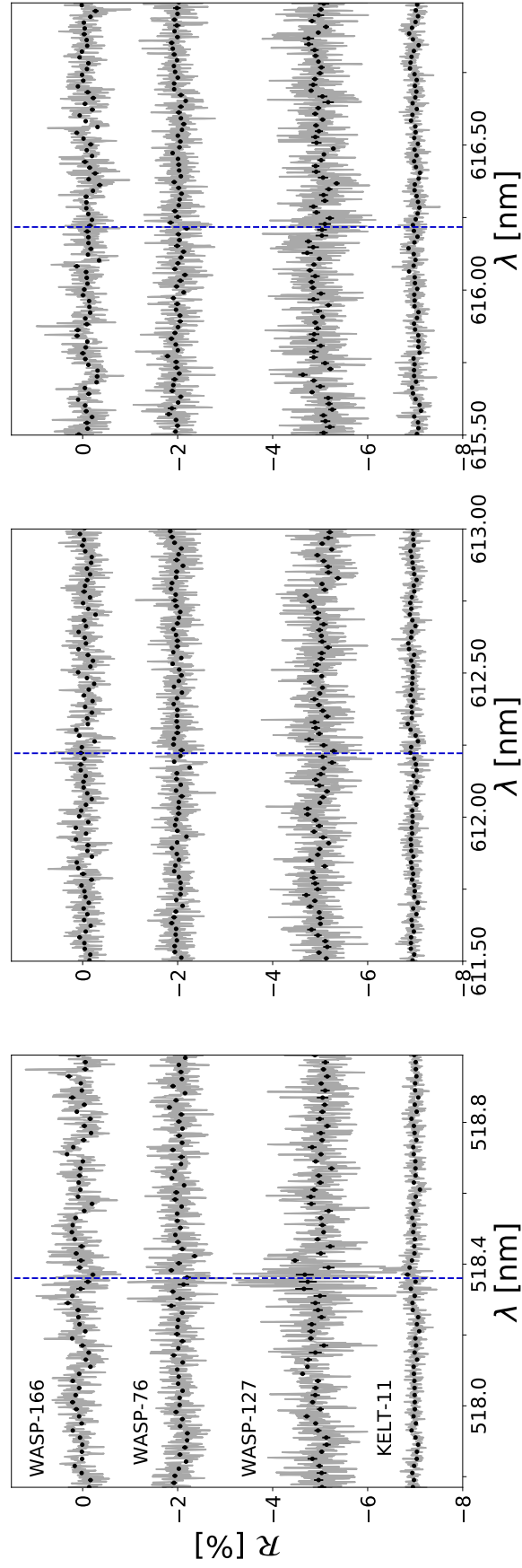


Figure 3.3: Activity cross-check region of the Ca I and Mg I lines for all of our targets. From left to right, the figure shows Mg I and both Ca I regions. Blue dashed lines indicate the exact position of the Mg I (518.3604 nm) and Ca I (612.2217 nm a 616.2173 nm) lines. The vertical offset was made for better readability ([Žák, et al., 2019](#)).

# Chapter 4

## Results and discussion

Each data set was analyzed for Na D (588.995 and 589.592 nm),  $H_\alpha$  (656.279 nm),  $H_\beta$  (486.135 nm) and Li (670.793 nm) to see the absorption in the exoatmosphere and for Ca I (612.222 and 616.217 nm) and Mg I (518.360 nm) to monitor the stellar activity. The results are discussed for each planet separately.

### 4.1 WASP-76b

Fig. 4.1 presents the final divided in/out transit spectra corrected for planetary radial velocity (gray) with the spectrum binned by 20 points (black) and a gaussian fit to the absorption lines (red). We can clearly see planetary sodium (Na D lines) absorption. The RMS of the Na D region is 0.0027 and the RMS of the spectrum binned by 20 is 0.0013. The sodium line depths are 0.65 % and 0.57 %, respectively, therefore, corresponding to  $9.5 \sigma$  and  $7.1 \sigma$  significance<sup>1</sup>. This is the first detection of sodium in the upper atmosphere of WASP-76b, originally published in [Žák, et al. \(2019\)](#). Details of the detected peaks are summarized in Table 4.1.

Figure 3.3 shows the non-detection of Ca I and Mg I lines (RMS of the data points is 0.0007), showing that the stellar activity is low and any planetary atmosphere sodium

Table 4.1: Fit parameters for the Na D lines in WASP-76b and WASP-127b.

Line	D1	D2
WASP-76b		
Depth (%)	$0.648 \pm 0.068$	$0.57 \pm 0.08$
FWHM (nm)	$0.0650 \pm 0.0078$	$0.0400 \pm 0.0065$
WASP-127b		
Depth (%)	$0.735 \pm 0.088$	$1.144 \pm 0.270$
FWHM (nm)	$0.0537 \pm 0.0075$	$0.0367 \pm 0.0097$

<sup>1</sup>The significance is calculated as the depth of the line divided by its uncertainty.

(Na D lines) detection should be significant and not influenced by the star.

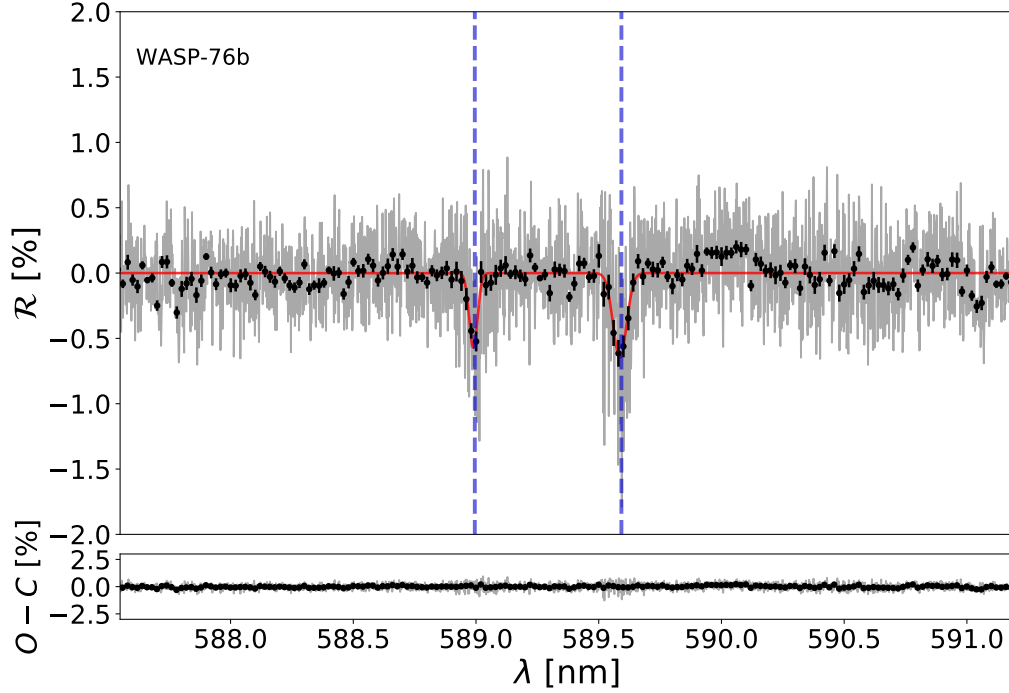


Figure 4.1: Spectral region around the sodium doublet of WASP-76b with stellar signature removed. The final transmission spectrum (gray), binned spectrum by 20 (black) and gaussian fit of the lines (red) are shown. Sodium is clearly detected, the blue dashed lines indicate the position of the Na D2 and D1 lines. The lower panels shows the difference between the observed spectrum and the fit (Žák, et al., 2019).

In the course of the review process of our work (Žák, et al., 2019), an independent detection of the sodium in the atmosphere of WASP-76b planet was reported by Seidel, et al. (2019) for the same HARPS data set. Their results are in agreement with ours, confirming the methodology. We note, however, that our FWHM of the D2 line is about 30 % smaller compared to their values which is probably caused by different approaches for the telluric correction. We do not detect any features in the positions of  $H\alpha$ ,  $H\beta$  or the lithium lines (Fig. A1). The lack of these features is possibly suggesting that the atmospheric loss is not prominent.

Furthermore, Ehrenreich, et al. (2020) observed WASP-76 system with the ESPRESSO instrument attached to the VLT and detected an iron signature on the day-side of the planet and reported no signal of the iron on the nightside. They provided an explanation of iron condensation on the nightside of the planet. von Essen, et al. (2020) detected sodium presence through low-resolution transmission spectroscopy using the *HST*/STIS. They also tentatively reported marginal evidence of titanium hydride. Using independent data sets they confirm our results of no planetary signal from  $H\beta$ ,  $H\alpha$  and lithium lines.

## 4.2 WASP-127b

A cloudless sky of WASP-127b was observed, several features such as sodium, potassium, and lithium and hints of H<sub>2</sub>O absorption were reported with GTC instrumentation by [Palle, et al. \(2017\)](#); [Chen, et al. \(2018\)](#). Fig. 4.2 presents our final transmission spectrum of the planet.

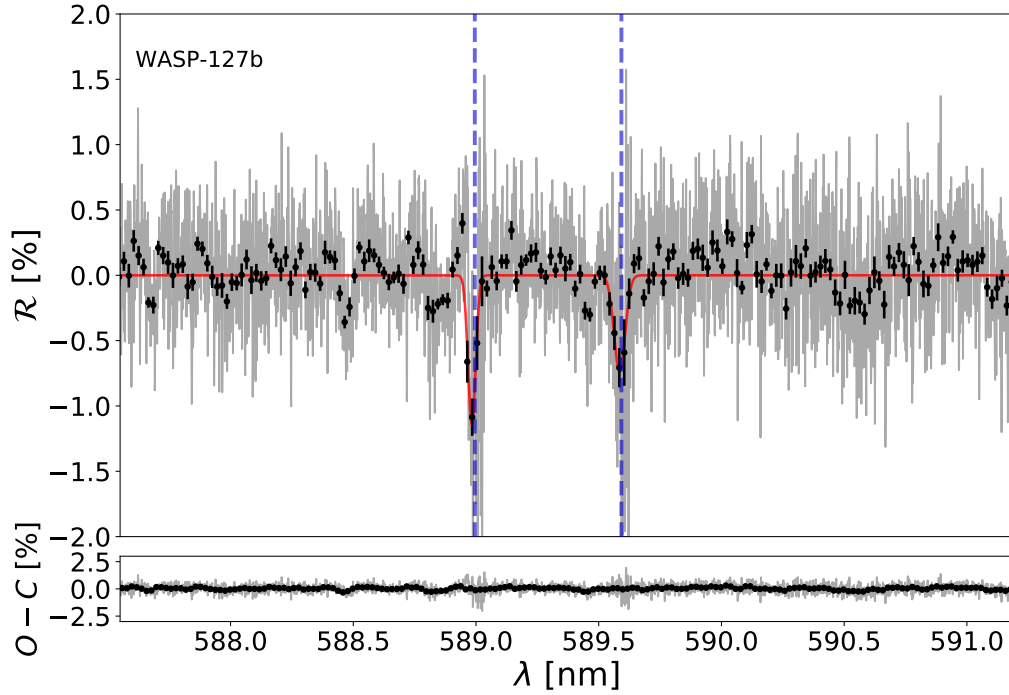


Figure 4.2: The same as Fig. 4.1 but for WASP-127b ([Žák, et al., 2019](#)).

The RMS of the data is 0.0042 and by binning by 20 points (black) we reach a final RMS of 0.0019. The stellar activity of WASP-127 star can be monitored with the Ca I and Mg I lines. We were not able to see any activity in these lines, as shown in Fig. 3.3. We were able to confirm only sodium (Na D lines) with a high significance of 4.2- $\sigma$  (D2) and 8.33- $\sigma$  (D1), respectively. Similarly to WASP-76b, we did not detect features of neutral hydrogen (H $\alpha$ , H $\beta$ ) or lithium (Fig. A1). Lithium was previously detected with low-resolution spectroscopy using the GTC as well as sodium and potassium ([Chen, et al., 2018](#)). The reason for our non-detection of lithium is most likely due to aperture differences between the GTC (10-m) and the 3.6-m telescope that hosts HARPS, while as mentioned earlier, potassium (766.5 & 769.9 nm) is out of range of HARPS.

Our confirmation of sodium is unique because this is one of the first proofs for observations using different instruments as well as two different methods. [Spake, et al. \(2019\)](#) used *HST* and *Spitzer* low-resolution data ranging from 0.3 to 5  $\mu$ m to detect feature-rich atmosphere. They independently confirm presence of sodium, potassium and water vapor. Additionally, they reported evidence of CO<sub>2</sub> in the transmission spectrum of WASP-127b for the first time. Finally, they reported no traces of lithium.

### 4.3 WASP-166b

Fig. 4.3 presents the final divided in/out transit spectrum for the Na region. The RMS of the data is 0.0025 and, after binning by 20 points, 0.0014. However, we are not able to detect any features in the sodium (Na D),  $H\beta$ ,  $H\alpha$  and lithium lines (Fig. A1). Therefore, we can only put an upper limit of 0.14 % on the detection.

As gas giant planets are expected to have nearly solar elemental composition (Madhusudhan, et al., 2016) the lack of features hints at presence of thick high clouds. High clouds are optically thick and thus only a small portion of the atmosphere, that is above the cloud deck, can be probed, thus resulting in a featureless spectrum. Another possible explanation for the featureless spectrum is the depletion of Na by its condensation on the night side of the planet (Seager, 2003). Future, follow-up studies with more sensitive instruments are thus recommended to investigate and break this degeneracy.

Fig. 3.3 displays no signatures in the Mg I and Ca I lines. Therefore, we can assume that the star is not active.

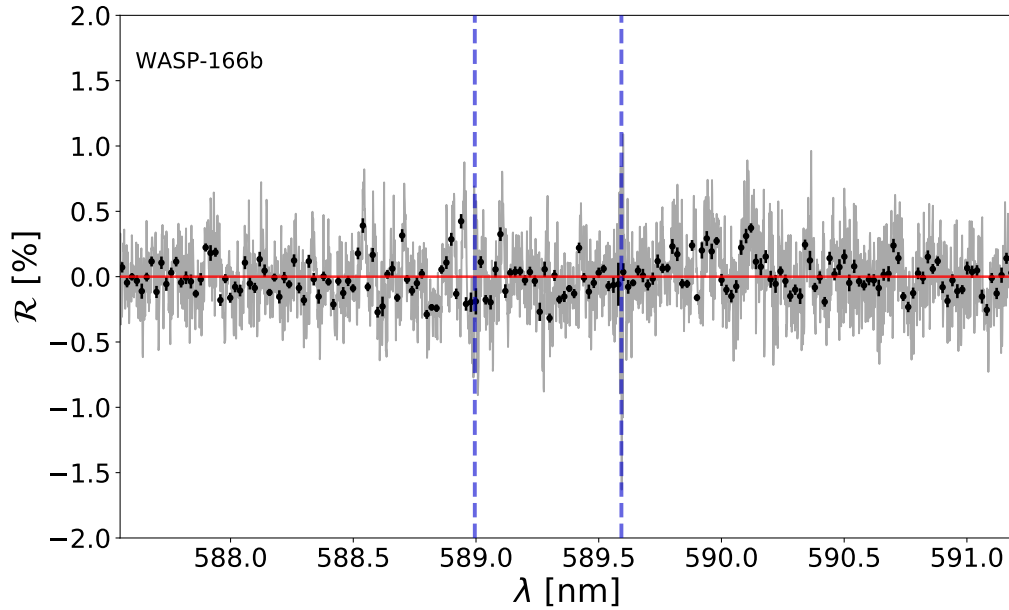


Figure 4.3: Same as Fig. 4.1, however, showing no-detection for WASP-166b (Žák, et al., 2019).

### 4.4 KELT-11b

Fig. 4.4 presents the final divided in/out transit spectrum of the Na region. The RMS of the data is 0.0012 (unbinned) and 0.0006 (binned by 20 points). The upper limit for sodium (Na D lines) detection is, therefore, 0.06 %. This is a very stringent constraint on the



presence of sodium in the atmosphere and possibly hints at the presence of clouds in the atmosphere of KELT-11b. Similarly to WASP-166b, we do not detect neutral hydrogen or lithium (Fig. A1).

We checked the stellar activity on Ca I and Mg I lines. There was no significant detection of activity observed in our data (see Fig. 3.3). Colón, et al. (2020) used *HST* low-resolution spectroscopy complemented with data from *TESS* and *Spitzer* to detect muted H<sub>2</sub>O feature in the IR region. The low amplitude H<sub>2</sub>O feature can be caused by partially cloudy atmosphere, however, the detected shape of the feature is unusual in comparison to other H<sub>2</sub>O features seen in giant planets. In the future, *JWST* observations could shed more light on processes in the atmosphere of this planet.

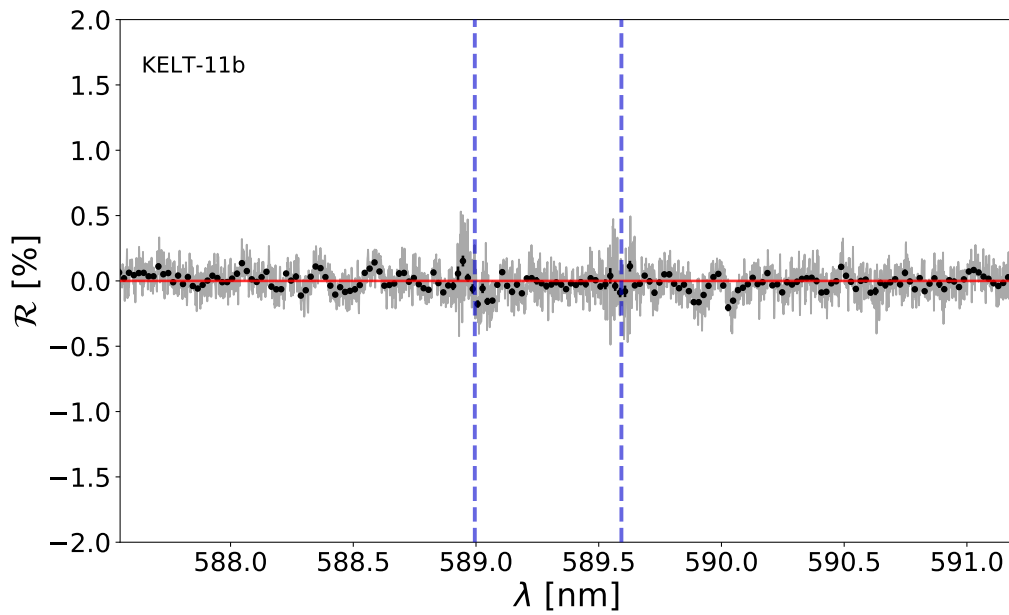


Figure 4.4: Same as Fig. 4.1, however, showing no-detection for KELT-11b (Žák, et al., 2019).

## 4.5 Discussion

We have performed transmission spectroscopy of 4 inflated gas giants and reported two successful detections of Na. WASP-76b belongs to the ultra-hot Jupiter class with intriguing iron-raining atmosphere (Ehrenreich, et al., 2020). WASP-127b with its cloudless atmosphere provides excellent opportunity to advance our understanding of super-Neptune’s atmospheres with *JWST* and future large-aperture facilities. The lack of atmospheric features in the spectra of WASP-166b and KELT-11b hints at the presence of clouds in large atmospheric heights. As high-resolution spectroscopy is sensitive to also higher atmospheric scale heights (Kempton, Perna & Heng, 2014), it can be used to detect features even in partially cloudy atmosphere.

As can be seen from Fig. 4.1, the D1 line is apparently stronger than the D2 line, which would imply different mixing ratios and compositions of the atmosphere of WASP-76b in comparison with other planets because all other detections reported in literature were with stronger D2 line. We have investigated the previous Na D line detections in exoplanets based on high-resolution spectroscopy in the literature. We have summarized them in Table 4.2. As can be seen, WASP-76b is the first reported planet having potentially an absorption ratio of D2 to D1 lines less than one<sup>2</sup>. The unusual reported values make this planet an ideal target for future *JWST* and large ground-based telescopes follow-up to further clarify this discovery.

Table 4.2: Selected high-resolution detections of sodium (Na D lines). The first column states the exoplanet with the source of the values. The second column shows the ratio of the sodium doublet absorption lines. The third column shows the ratio of the sodium doublet FWHMs.

Planet	$A_{D2}/A_{D1}$	$f_{D2}/f_{D1}$
HD 189733b <sup>1</sup>	$1.59 \pm 0.33$	$1 \pm 0.22$
WASP-49b <sup>2</sup>	$1.09 \pm 0.47$	$1.91 \pm 0.83$
MASCARA-2b <sup>3</sup>	$1.19 \pm 0.39$	$0.79 \pm 0.31$
WASP-17b <sup>4</sup>	$1 \pm 0.66$	$1 \pm 0.57$
WASP-52b <sup>5</sup>	$1.20 \pm 0.21$	$1.88 \pm 0.31$
WASP-127b <sup>6</sup>	$1.56 \pm 0.41$	$0.68 \pm 0.20$
WASP-76b <sup>6</sup>	$0.88 \pm 0.15$	$0.62 \pm 0.12$

**References:** (1) [Wytttenbach, et al. \(2015\)](#), (2) [Wytttenbach, et al. \(2017\)](#), (3) [Casasayas-Barris, et al. \(2018\)](#), (4) [Khalafinejad, et al. \(2018\)](#), (5) [Chen, et al. \(2020\)](#), (6) [Žák, et al. \(2019\)](#)

The explanation for the strength of the lines can be found in the literature for other Na lines in redder regions but such a measurement is missing in the optical. [Civiš, et al. \(2012\)](#) present a laboratory spectrum of sodium lines demonstrating that different atomic states are shaping the spectral lines and their strengths. Furthermore, [Slanger, et al. \(2005\)](#) measured the D2/D1 ratio in the Earth's atmosphere and found it to be varying between 1.2-1.8. They explained that the variability of the ratio is originating from a competition between oxygen reacting with  $\text{NaO}(A^3\Sigma^+)$ , produced from the reaction of sodium with oxygen. In other words, the line strength and the mixing ratio depend on the composition of the surrounding atmosphere and it can even vary over time.

<sup>2</sup>One should note, however, that the deviation from unity is less than  $1\sigma$  for WASP-76b, and we therefore do not claim much about this yet. Several detections have the reported ratio close to unity with large uncertainty, thus further research is needed to properly address the uncertainties.

# Chapter 5

## Future prospects

In the near future several space missions designed for exoplanetary research will be launched. They will be complemented by large ground-based observatories.

### 5.1 Future projects

#### James Webb Space Telescope

James Webb Space Telescope (*JWST*, [Gardner, et al., 2006](#)) is a planned space telescope that is scheduled to be launched in 2021. The primary mirror will consist of 18 hexagonal segments that are equal to a 6.5-m single mirror. It will operate in the region from 0.6 to 28.3  $\mu\text{m}$ . By employing four instruments (NIRSpec, NIRISS, NIRCams, and MIRI) it will be capable of achieving resolving power  $R \sim 100\text{--}1700$ . The spectral ranges of the instruments are shown in Fig. 5.1 together with cross-sections of various molecules. Its main scientific objectives will be to investigate the early universe by studying objects that formed shortly after the Big Bang. It will study the formation and evolution of galaxies, stars, and exoplanets. Characterization of exoatmospheres is also a significant part of the Early Release Science (ERS) Program ([Stevenson, et al., 2016](#)) for which data will be obtained during the first five months of observations.

#### ARIEL

The Atmospheric Remote-sensing Infrared Exoplanet Large-survey (*ARIEL*, [Tinetti, et al., 2016](#)) is an ESA M-4 mission planned to be launched in 2028. The mission is expected to perform observations of at least 1000 exoplanets. It will be equipped with a 1.1 x 0.7-m oval mirror to carry out spectroscopic measurements in the NIR and IR regions (1.2  $\mu\text{m}$  to 7.8  $\mu\text{m}$ ). Two main scientific questions that *ARIEL* will address are: *What are exoatmospheres made of?* and *How do planets form and evolve?* To achieve this *ARIEL* will characterize the chemical composition of exoatmospheres. *ARIEL* is expected to detect molecular bands  $\text{H}_2\text{O}$ ,  $\text{HCN}$ ,  $\text{CO}_2$ ,  $\text{NH}_3$  and many others. Furthermore, it will provide information about the atmospheric structure, chemical gradients as well as clouds and albedo measurements.

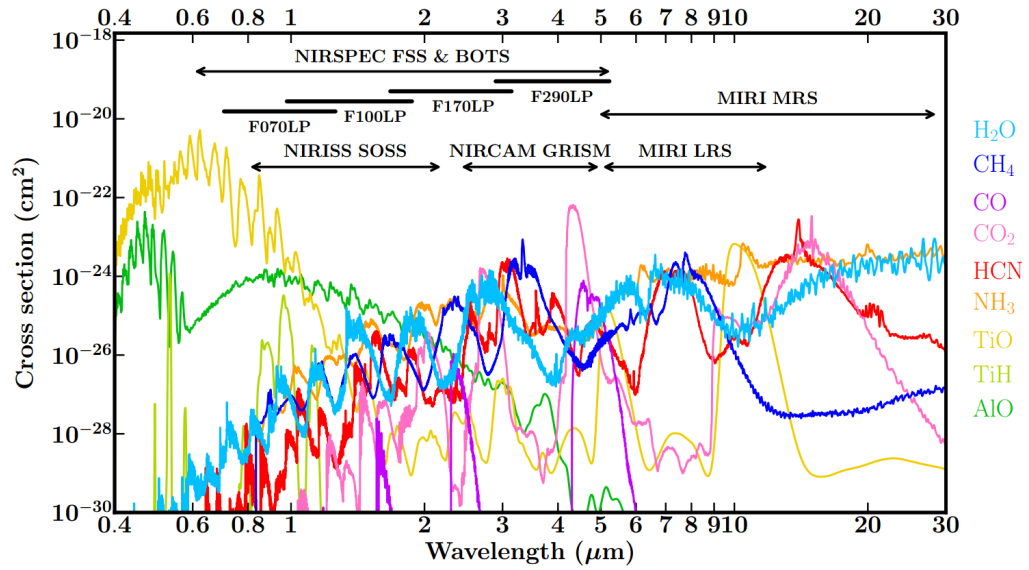


Figure 5.1: Cross-sections of various molecules across optical and infrared wavelengths for *JWST*. Spectral ranges covered by certain modes of *JWST*'s four instruments (NIRSpec, NIRISS, NIRCams, and MIRI) are shown for comparison. For NIRSpec, the wavelength coverage of individual filters is also shown. *JWST*'s extensive spectral coverage will enable detailed chemical characterizations of exoplanetary atmospheres. Taken from [Madhusudhan \(2019\)](#).

## CUTE

The Colorado Ultraviolet Transit Experiment (*CUTE*, [Fleming, et al., 2018](#)) will be a CubeSat with a 20x8-cm parabolic mirror. It is a joint project of Colorado and Graz University. It will perform low-resolution transmission spectroscopy in the near-ultraviolet region from 255 to 330 nm. It will search for atmospheric tracers (Fe II, Mg II, Mg I and OH) that cannot be studied from the ground. The expected launch is 2020.

## PLATO

PLANetary Transits and Oscillations of stars (*PLATO*, [Rauer, et al., 2014, 2016](#)) is the planned space mission by the ESA to be launched in 2026. *PLATO* will be a photometric mission and will have onboard 26 refracting telescopes. Twentyfour normal cameras with readout cadence of 25 s in groups of 4 for stars with brightness between 8 and 16 in *V* mag; 2 fast cameras with readout cadence of 2.5 s and color filters for bright stars (4-8 in *V* mag). The 24 normal cameras will have field of view of about 2250 squared degrees. The main goal is to discover Earth-like planets in the habitable zone around Sun-like star. Furthermore, it will address questions such as *What are the properties of exoplanets?* and *How do planets systems evolve with age?*. The mission will be valuable also for astroseismology as *PLATO* will investigate stellar structure and evolution. Most importantly for exoatmosphere research, it will deliver many suitable candidates for exoatmosphere characterization.

### Roman Space Telescope

Nancy Grace Roman Space Telescope (*Roman*, formerly known as *WFIRST*) is infrared observatory currently under development (Spergel, et al., 2015; Akeson, et al., 2019). The expected launch is 2025. The observatory will have 2.4-m telescope with two scientific instruments. The first instrument is the 288-megapixel multi-band NIR camera with 100 times larger field of view than *HST*. It will be capable of wide-field slitless spectroscopy and imaging in the optical and IR region. The coronagraph instrument with a high contrast will perform imaging and integral field spectroscopy. The main objectives of the *Roman* will be to study the expansion history of the Universe, the growth of cosmic structure and the dark energy. Furthermore, its coronagraph will be used for direct imaging of exoplanets that will provide images (see Fig. 5.2) and spectra of the near exoplanets. The design will enable detection of exoplanets only 0.15 arcseconds away from their host star.

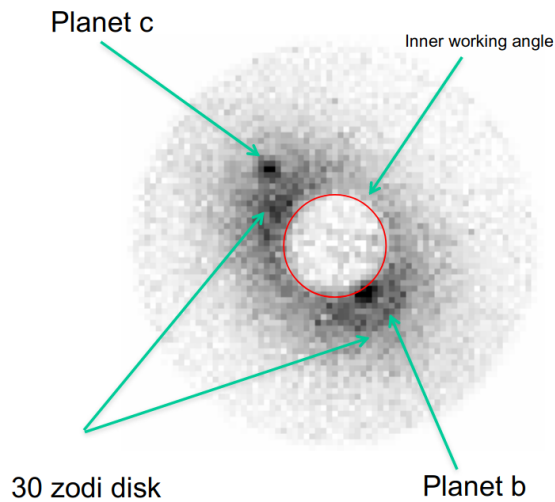


Figure 5.2: Simulated *Roman* coronagraph image of the star 47 Ursae Majoris, showing two directly detected planets with 10 hr exposure (Spergel, et al., 2015).

### CRIRES+

CRIRES+ (Dorn, et al., 2016) is an upgrade of The CRyogenic InfraRed Echelle Spectrograph (CRIRES). It is a cross-dispersed spectrograph that is as of May 2020 being installed on VLT. It will be equipped with 6 gratings each optimized for operation in a single wavelength band (*Y*, *J*, *H*, *K*, *L* and *M*). It will be able to achieve resolving power of  $R=50\,000$ - $100\,000$ . It will have a new polarimetry module allowing spectropolarimetric observations. One of the main scientific objectives will be to search for super-Earths in the habitable zone of low-mass stars. Due to the low temperature of M-dwarfs, they radiate most of their energy in the IR region. Thus CRIRES+ is a perfect instrument for this task.

Another scientific objective will be the atmospheric characterization of exoplanetary atmospheres. As was described in section 1.3, IR region is suitable for atmospheric detection of helium and molecular bands e.g.  $\text{H}_2\text{O}$ ,  $\text{CO}$ ,  $\text{NH}_3$ ,  $\text{CH}_4$ .

### Giant ground-based observatories

**Extremely Large Telescope** (ELT, [de Zeeuw, Tamai & Liske, 2014](#)) is an astronomical observatory currently under construction. Once completed it will be the largest optical telescope ever built. In 2010 ESO selected Cerro Armazones as the telescope site and in 2014 construction begun. The expected first-light is currently planned in 2025. ELT will use optical design with 5 mirrors. The 39-m primary mirror will consist of 798 hexagonal segments, each segment measuring approximately 1.4-m across. Multiple instruments will be suitable for the investigation of exoplanets. The High Angular Resolution Monolithic Optical and Near-infrared Integral field Spectrograph (HARMONI) is a planned spectrograph that will operate in region from 0.47 to  $2.45\ \mu\text{m}$  with resolving power  $R \sim 3\,000 - 20\,000$ . High Resolution Spectrograph (HIRES, [Di Varano, et al., 2019](#)) is planned spectrograph currently under review. It will operate simultaneously in the optical and NIR region with  $R \sim 100\,000$ . The primary goal of HIRES will be the characterization of exoplanetary atmospheres. ELT should be able to directly detect oxygen.



Figure 5.3: The visualisation of the Extremely Large Telescope. Image credit: ESO.

**Thirty Meter Telescope** (TMT, [Schöck, et al., 2009](#)) is a proposed telescope to be located on Mauna Kea, Hawaii. Recently, due to the blockade on Mauna Kea, alternate sites were considered, especially Roque de los Muchachos observatory on La Palma. The primary mirror is designed to have 30-m in diameter and will consist of 492 smaller (1.4-m) individual segments. Planned instruments include High-resolution spectrographs in the visible domain (HROS), and near-infrared (NIREs).



**Giant Magellan Telescope** (GMT, [Fanson, et al., 2018](#)) is future telescope currently under construction at Las Campanas observatory in Chile. The primary mirror will consist of seven 8.4-m segments forming 25.4-m primary mirror. The first light is planned for 2029. The secondary mirror will be equipped with adaptive optics to correct distortions caused by Earth's atmosphere. GMT will be equipped with high-resolution spectrographs for visible and IR region (G-CLEF and GMTNIRS) enabling very precise exoatmosphere characterization.

## 5.2 Future plans

### JWST is coming...

With the upcoming projects like *JWST*, *ELT*, *TMT* and many others, the golden area of characterization of exoatmospheres is yet to begin. These projects will greatly benefit from the preparatory scientific work that can already be carried out. *JWST* will have good coverage of the IR region thus ground-based telescopes can provide complementary information that can be firstly used for selection of the best candidates and subsequently to complement atmospheric retrieval in further studies.

Clouds and hazes hinder the ability to retrieve planetary signals, thus, it is important to know whether clouds/hazes are present. For example, WASP-101b was considered a prime target for the Early Release Science (ERS) program, however, [Wakeford, et al. \(2017b\)](#) have shown the planet is obscured by clouds. Similarly, KELT-11b and WASP-166b were promising targets however our study has revealed featureless spectra. [Heng \(2016\)](#) suggested that the amplitude of the [Na/K] line center relative to their adjacent continua can be used to constrain the cloudiness of the planet.

We plan to use ESPRESSO instrument ([Pepe, et al., 2014](#); [González Hernández, et al., 2018](#)) to obtain the complete optical spectrum of several targets that are anticipated to be included in the ERS Program. As ESPRESSO has coverage of the optical 650 nm and 740 nm H<sub>2</sub>O bands, the scientific objective will also be to detect H<sub>2</sub>O band in the optical region for the first time. It was shown by [Allart, et al. \(2017\)](#) that by using the CCF method, the H<sub>2</sub>O detection is possible. These results can be directly compared to the measurement from the IR bands measured by *JWST* and/or other missions. In addition to H<sub>2</sub>O, we will search for signatures of Na, K, Li, neutral hydrogen and other atmospheric features.

For the temperature ranges of the selected planets based on theoretical models ([Fortney, et al., 2008](#)) and previous detections ([Wytenbach, et al., 2015, 2017](#); [Khalafinejad, et al., 2018](#)) we expect strong signals from the sodium and potassium. Detection or non-detection of these alkali metals will be used to lift degeneracy of chemical and physical properties in the retrieval analysis (Fig. 5.4). Ultra-hot Jupiters are known to exhibit atmospheric escape which can be conveniently studied using the H $\alpha$  line ([Casasayas-Barris, et al., 2019](#)). Detection of H $\alpha$  can be explained by a very high temperature of the outer layer of the atmosphere. However, [Chen, et al. \(2020\)](#) have shown that neutral hydrogen can be detected also for non-ultra-hot Jupiters. Possible detection of TiO will be able to provide excellent temperature constraint as TiO becomes a prominent absorber in the optical for higher temperatures ([Fortney, et al., 2008](#)).

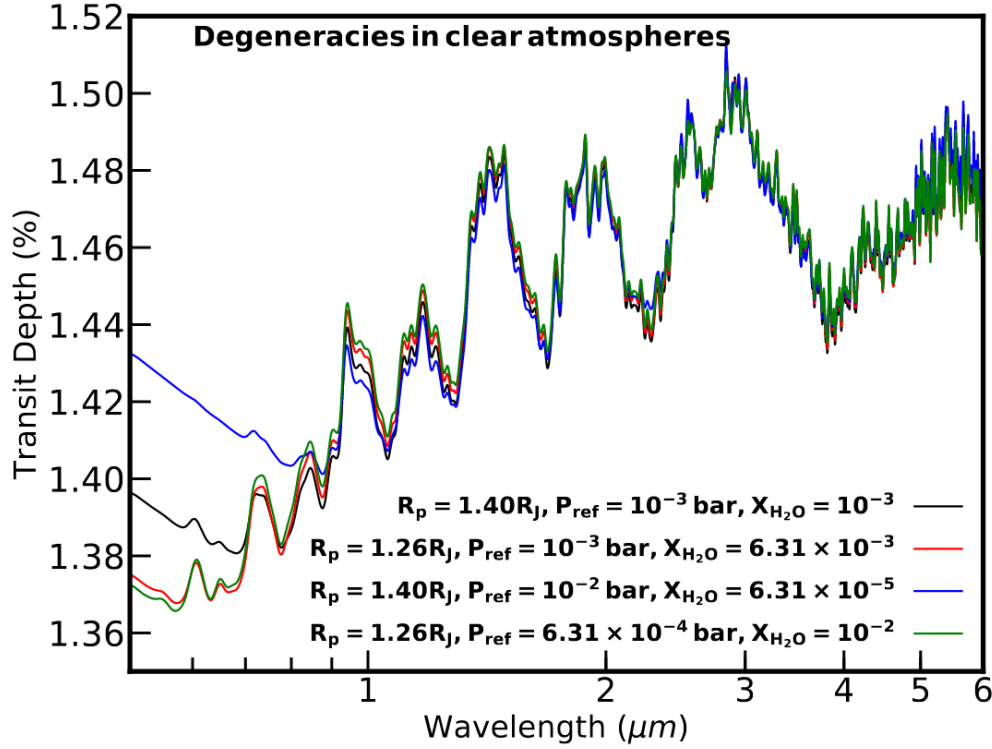


Figure 5.4: Atmospheric spectra with different chemical composition and physical properties (Welbanks & Madhusudhan, 2019). These spectra have a similar absorption features in the NIR region. By obtaining optical data with VLT/ESPRESSO we will be able to lift these degeneracies and be able to precisely constrain the composition of the atmosphere.

For our future project, we have used a similar approach as described in Chapter 2 to identify candidates for exoatmosphere characterization. We select candidates with extended atmospheres around bright stars. We also take into account if the candidate was selected or is considered for the ERS Program. We present our 3 candidates in Table 5.1.

WASP-62b is a hot Jupiter orbiting a bright F-type star. Its detection was reported by Hellier, et al. (2012) who reported no emission peaks in the Ca II H+K lines hinting at a low stellar activity. Stevenson, et al. (2016) identified this target as one of the most favorable for the upcoming ERS *JWST* program as it is located in the *JWST*'s continuous viewing zone thus resulting in a large number of transit opportunities at any time of the year for *JWST*. There are still no atmospheric observations available for this candidate.

Hellier, et al. (2012) reported a discovery of a hot Jupiter WASP-63b orbiting a G-type star. They did not find any signs of stellar activity. Kilpatrick, et al. (2018) studied this planet using single transit data from *HST*. They detected H<sub>2</sub>O in the IR region and conclude that WASP-63b remains a plausible target for ERS.

WASP-79b is another hot Jupiter in our sample. Smalley, et al. (2012) reported its discovery around a F-type star. WASP-79b is the prime candidate for the ERS program (Bean, et al., 2018). Sotzen, et al. (2020) analyzed data from *Spitzer*, *HST*, LDSS-3C instrument mounted at Magellan telescope, and *TESS* and constrained H<sub>2</sub>O abundance. However, atmospheric data, especially in the optical region, are still missing.



Table 5.1: Parameters of selected targets for complementary science to *JWST* with ESPRESSO.

	WASP-62b	WASP-63b	WASP-79b
Mass ( $M_{\text{Jup}}$ )	0.57	0.38	0.9
Radius ( $R_{\text{Jup}}$ )	1.39	1.43	1.7
Temperature (K)	1440	1540	1760
Period (d)	4.412	4.378	3.662
Semi-major axis (AU)	0.0567	0.0574	0.0539
$V$ (mag)	10.3	11.2	10.1
$1000 \cdot \Delta\delta$	1.10	0.90	0.96

**CRIRES+ science verification**

CRIRES+ science verification call is expected in the second half of 2020 which will allow scientists to test capabilities of this new instrument. In the next project, we would like to use CRIRES+ to detect helium in the atmosphere of gas giant exoplanet. We will use the strong  $\lambda 1083.3$  nm helium triplet which has already been detected in several planets (Nortmann, et al., 2018; Allart, et al., 2019). Helium IR triplet together with Lyman-alpha ( $\text{Ly}\alpha$ ) line can be used to study atmospheric escape. However,  $\text{Ly}\alpha$  can be detected only from space with the *HST* instrument and is heavily affected by the interstellar absorption. The helium IR triplet thus provides an excellent opportunity to study the atmospheric escape of irradiated planets and their mass-loss (Lampón, et al., 2020).

# Chapter 6

## Conclusions

In this thesis, we first selected suitable targets for high-resolution transmission spectroscopy. We identified 4 gas giant planets with hot extended atmospheres around bright stars which makes them ideal targets for atmospheric characterization (WASP-76b, WASP-127b, KELT-11b, and WASP-166b). We analyzed HARPS archival data from the ESO archive. After performing telluric correction, we searched for planetary features in the atmospheres of the planets. We ruled out the presence of any spurious signals caused by the stellar activity by monitoring the Mg I and Ca I lines. We detect sodium in the atmosphere of WASP-76b at a  $7-9\sigma$  level. Furthermore, we also report the detection of sodium in the atmosphere of WASP-127b at a  $4-8\sigma$  level of significance, confirming earlier results based on low-resolution spectroscopy. This is one of the first cases of detecting the same atmospheric feature using different instruments as well as two different methods. We also searched for the presence of neutral hydrogen ( $H\alpha$  and  $H\beta$ ) which could be a sign of the escaping atmosphere and lithium (670.8 nm), however, no features were detected. The lithium presence in the atmosphere of WASP-127b was detected using the low-resolution technique from the ground, however was not confirmed with the same method from space. The data show no sodium nor presence of any other atom at high confidence levels for WASP-166b nor KELT-11b, hinting at the presence of thick high clouds in the atmospheres of these two exoplanets.

Furthermore, we report an unusual sodium depth ratio of the D2 and D1 lines in WASP-76b. By analyzing other detections of sodium in different exoplanets available in literature we conclude that this is the first detection of possibly inverted sodium doublet ratio. Further investigation of this phenomenon is currently ongoing. In the near future, optical transmission spectroscopy will be very valuable as it will be complementary for the upcoming missions like *JWST* and *ARIEL*. Optical data from instruments such as ESPRESSO, HARPS, FORS2 will lift degeneracies that are present in the chemical composition retrieval and atmospheric processes description from the NIR data.

Since the publication of our paper (Žák, et al., 2019), our results of atmosphere detection for WASP-76b and WASP-127b and non-detection for WASP-166b and KELT-11b have already been cited by several studies (Chen, et al., 2020; Colón, et al., 2020; Edwards, et al., 2020; von Essen, et al., 2020), showing the importance and a good timing of our investigation. We finish with an outlook on how we want to move forward with exoatmosphere characterization by introducing two feasible projects in the near future.

**Related publications:**

**Žák, J.**, Kabáth, P., Boffin, H. M. J., Ivanov, V. D., Skarka, M. 2019. *High-resolution Transmission Spectroscopy of Four Hot Inflated Gas Giant Exoplanets*. The Astronomical Journal 158, 120.

Kabáth, P., **Žák, J.**, Boffin, H. M. J., Ivanov, V. D., Jones, D., Skarka, M. 2019. *Detection Limits of Exoplanetary Atmospheres with 2-m Class Telescopes*. Publications of the Astronomical Society of the Pacific 131, 085001.

# Bibliography

- Addison B. C., Tinney C. G., Wright D. J., Bayliss D., 2016, ApJ, 823, 29
- Akeson R., et al., 2019, arXiv, arXiv:1902.05569
- Allart R., Lovis C., Pino L., Wyttenbach A., Ehrenreich D., Pepe F., 2017, A&A, 606, A144
- Allart R., et al., 2019, A&A, 623, A58
- Astudillo-Defru N., Rojo P., 2013, A&A, 557, A56
- Baglin A., et al., 2002, ESASP, 485, 17, ESASP.485
- Bakos G., Noyes R. W., Kovács G., Stanek K. Z., Sasselov D. D., Domsa I., 2004, PASP, 116, 266
- Ballard S., et al., 2011, ApJ, 743, 200
- Barman T. S., Konopacky Q. M., Macintosh B., Marois C., 2015, ApJ, 804, 61
- Bashi D., Helled R., Zucker S., Mordasini C., 2017, A&A, 604, A83
- Bean J. L., et al., 2018, PASP, 130, 114402
- Beaulieu J.-P., et al., 2006, Natur, 439, 437
- Beichman C., et al., 2019, BAAS, 51, 58
- Benneke B., et al., 2019, ApJL, 887, L14
- Bernstein R., Shectman S. A., Gunnels S. M., Mochnacki S., Athey A. E., 2003, SPIE, 4841, 1694, SPIE.4841
- Bertaux J.-L., et al., 2007, Natur, 450, 646
- Bida T. A., Killen R. M., Morgan T. H., 2000, Natur, 404, 159
- Birkby J. L., de Kok R. J., Brogi M., de Mooij E. J. W., Schwarz H., Albrecht S., Snellen I. A. G., 2013, MNRAS, 436, L35
- Boffin H. M. J., et al., 2016, SPIE, 9908, 99082B, SPIE.9908

- Bouchy F., Doyon R., Pepe F., Wildi F., Blind N., Artigau E., Malo L., 2019, EPSC, 2019, EPSC-DPS2019-1860
- Bourrier V., et al., 2013, A&A, 551, A63
- Borucki W. J., et al., 2010, Sci, 327, 977
- Broadfoot A. L., et al., 1981, JGR, 86, 8259
- Brogi M., Snellen I. A. G., de Kok R. J., Albrecht S., Birkby J. L., de Mooij E. J. W., 2013, ApJ, 767, 27
- Brown D. J. A., et al., 2017, MNRAS, 464, 810
- Butler R. P., Marcy G. W., Williams E., McCarthy C., Dosanji P., Vogt S. S., 1996, PASP, 108, 500
- Butler R. P., et al., 2017, AJ, 153, 208
- Burgdorf M., Orton G., van Cleve J., Meadows V., Houck J., 2006, Icar, 184, 634
- Campbell B., Walker G. A. H., Yang S., 1988, ApJ, 331, 902
- Casasayas-Barris N., Palte E., Nowak G., Yan F., Nortmann L., Murgas F., 2017, A&A, 608, A135
- Casasayas-Barris N., et al., 2018, A&A, 616, A151
- Casasayas-Barris N., et al., 2019, A&A, 628, A9
- Carter A. L., et al., 2020, MNRAS, 494, 5449
- Cegla H. M., Lovis C., Bourrier V., Watson C. A., Wyttenbach A., 2017, A&A, 598, L3
- Charbonneau D., Brown T. M., Latham D. W., Mayor M., 2000, ApJL, 529, L45
- Charbonneau D., Brown T. M., Noyes R. W., Gilliland R. L., 2002, ApJ, 568, 377
- Chen G., et al., 2018, A&A, 616, A145
- Chen G., et al., 2020, A&A, 635, A171
- Civiš S., Ferus M., Kubelík P., Jelinek P., Chernov V. E., Zanozina E. M., 2012, A&A, 542, A35
- Chilcote J., et al., 2017, AJ, 153, 182
- Claudi R., et al., 2017, EPJP, 132, 364
- Colón K. D., Ford E. B., Redfield S., Fortney J. J., Shabram M., Deeg H. J., Mahadevan S., 2012, MNRAS, 419, 2233
- Colón K. D., et al., 2020, arXiv, arXiv:2005.05153

- Cosentino R., et al., 2012, SPIE, 8446, 84461V, SPIE.8446
- Courtin R., Gautier D., Marten A., Bezard B., 1983, BAAS, 15, 831
- Damiano M., Morello G., Tsiaras A., Zingales T., Tinetti G., 2017, AJ, 154, 39
- Dekker H., D’Odorico S., Kaufer A., Delabre B., Kotzlowski H., 2000, SPIE, 4008, 534, SPIE.4008
- Deming D., et al., 2013, ApJ, 774, 95
- Deming D., Louie D., Sheets H., 2019, PASP, 131, 013001
- de Zeeuw T., Tamai R., Liske J., 2014, Msngr, 158, 3
- Di Varano I., Yuan S., Woche M., Strassmeier K. G., Weber M., 2019, SPIE, 11057, 1105715, SPIE11057
- Dorn R. J., et al., 2016, SPIE, 9908, 99080I, SPIE.9908
- Dumusque X., et al., 2019, A&A, 627, A43
- Edwards B., et al., 2020, arXiv, arXiv:2005.02374
- Ehrenreich D., et al., 2015, Natur, 522, 459
- Ehrenreich D., et al., 2020, arXiv, arXiv:2003.05528
- Espinoza N., et al., 2019, MNRAS, 482, 2065
- Evans T. M., et al., 2016, ApJL, 822, L4
- Evans T. M., et al., 2017, Natur, 548, 58
- Fanson J., et al., 2018, SPIE, 10700, 1070012, SPIE10700
- Fischer P. D., et al., 2016, ApJ, 827, 19
- Fisher C., Heng K., 2019, ApJ, 881, 25
- Fleming B. T., et al., 2018, JATIS, 4, 014004
- Formisano V., Atreya S., Encrenaz T., Ignatiev N., Giuranna M., 2004, Sci, 306, 1758
- Fortney J. J., Lodders K., Marley M. S., Freedman R. S., 2008, ApJ, 678, 1419
- Franz H. B., et al., 2017, P&SS, 138, 44
- Fraine J., et al., 2014, Natur, 513, 526
- Fu G., Deming D., Knutson H., Madhusudhan N., Mandell A., Fraine J., 2017, ApJL, 847, L22
- Gandhi S., Madhusudhan N., 2019, MNRAS, 485, 5817

- Gardner J. P., et al., 2006, SSRv, 123, 485
- Gaudi B. S., et al., 2017, Natur, 546, 514
- González Hernández J. I., Pepe F., Molaro P., Santos N. C., 2018, haex.book, 157, haex.book
- Griffin R., 1973, MNRAS, 162, 243
- Hatzes A. P., Cochran W. D., 1992, ESOC, 40, 275, ESOC...40
- Hatzes A. P., et al., 2003, ApJ, 599, 1383
- Hatzes A. P., Rauer H., 2015, ApJL, 810, L25
- Hawker G. A., Madhusudhan N., Cabot S. H. C., Gandhi S., 2018, ApJL, 863, L11
- Haynes K., Mandell A. M., Madhusudhan N., Deming D., Knutson H., 2015, ApJ, 806, 146
- Heintz W. D., 1978, ApJ, 220, 931
- Hellier C., et al., 2012, MNRAS, 426, 739
- Hellier C., et al., 2019, MNRAS, 488, 3067
- Heng K., 2016, ApJL, 826, L16
- Henry G. W., Marcy G. W., Butler R. P., Vogt S. S., 2000, ApJL, 529, L41
- Hoeijmakers H. J., et al., 2018, Natur, 560, 453
- Hoeijmakers H. J., et al., 2019, A&A, 627, A165
- Hubbard W.B., 1997, Sci, 275, 5304
- Hubeny I., Burrows A., Sudarsky D., 2003, ApJ, 594, 1011
- Hueso R., et al., 2020, Icar, 336, 113429
- Huitson C. M., et al., 2013, MNRAS, 434, 3252
- Janson M., et al., 2013, ApJL, 778, L4
- Jensen A. G., Redfield S., Endl M., Cochran W. D., Koesterke L., Barman T., 2012, ApJ, 751, 86
- Jones M. I., et al., 2019, A&A, 625, A16
- Kabáth P., Žák J., Boffin H. M. J., Ivanov V. D., Jones D., Skarka M., 2019, PASP, 131, 085001
- Keles E., et al., 2019, MNRAS, 489, L37

- Kempton E. M.-R., Perna R., Heng K., 2014, *ApJ*, 795, 24
- Khalafinejad S., et al., 2018, *A&A*, 618, A98
- Kilpatrick B. M., et al., 2018, *AJ*, 156, 103
- Killen R., et al., 2007, *SSRv*, 132, 433
- Kirk J., et al., 2019, *AJ*, 158, 144
- Konopacky Q. M., Barman T. S., Macintosh B. A., Marois C., 2013, *Sci*, 339, 1398
- Kreidberg L., et al., 2014, *ApJL*, 793, L27
- Kreidberg L., et al., 2015, *ApJ*, 814, 66
- Latham D. W., Mazeh T., Stefanik R. P., Mayor M., Burki G., 1989, *Natur*, 339, 38
- Lam K. W. F., et al., 2017, *A&A*, 599, A3
- Lampón M., et al., 2020, *arXiv*, arXiv:2003.04872
- MacDonald R. J., Madhusudhan N., 2017, *MNRAS*, 469, 1979
- Madhusudhan N., Agúndez M., Moses J. I., Hu Y., 2016, *SSRv*, 205, 285
- Madhusudhan N., 2019, *ARA&A*, 57, 617
- Mandell A. M., Haynes K., Sinukoff E., Madhusudhan N., Burrows A., Deming D., 2013, *ApJ*, 779, 128
- Mayor M., Queloz D., 1995, *Natur*, 378, 355
- Mayor M., et al., 2003, *Msngr*, 114, 20
- Marois C., et al., 2008, *Sci*, 322, 1348
- McCullough P. R., Crouzet N., Deming D., Madhusudhan N., 2014, *ApJ*, 791, 55
- McLaughlin D. B., 1924, *ApJ*, 60, 22
- Montañés-Rodríguez P., González-Merino B., Pallé E., López-Puertas M., García-Melendo E., 2015, *ApJL*, 801, L8
- Nikolov N., et al., 2016, *ApJ*, 832, 191
- Nikolov N., et al., 2018, *Natur*, 557, 526
- Noll K. S., et al., 1995, *Sci*, 267, 1307
- Noguchi K., et al., 2002, *PASJ*, 54, 855
- Nortmann L., et al., 2018, *Sci*, 362, 1388



- Nugroho S. K., Kawahara H., Masuda K., Hirano T., Kotani T., Tajitsu A., 2017, *AJ*, 154, 221
- Otegi J. F., Bouchy F., Helled R., 2020, *A&A*, 634, A43
- Pallé E., Zapatero Osorio M. R., Barrena R., Montañés-Rodríguez P., Martín E. L., 2009, *Natur*, 459, 814
- Palle E., et al., 2017, *A&A*, 602, L15
- Palle E., et al., 2020, *arXiv*, arXiv:2004.12812
- Pepe F., et al., 2014, *arXiv*, arXiv:1401.5918
- Pepper J., et al., 2007, *PASP*, 119, 923
- Pepper J., et al., 2017, *AJ*, 153, 215
- Perryman M., 2018, *exha.book*
- Pollacco D. L., et al., 2006, *PASP*, 118, 1407
- Queloz D., et al., 2000, *A&A*, 359, L13
- Schöck M., et al., 2009, *PASP*, 121, 384
- Rauer H., et al., 2014, *ExA*, 38, 249
- Rauer H., Aerts C., Cabrera J., PLATO Team, 2016, *AN*, 337, 961
- Redfield S., Endl M., Cochran W. D., Koesterke L., 2008, *ApJL*, 673, L87
- Ricker G. R., et al., 2015, *JATIS*, 1, 014003
- Rossiter R. A., 1924, *ApJ*, 60, 15
- Rothman L. S., et al., 2013, *JQSRT*, 130, 4
- Salz M., et al., 2018, *A&A*, 620, A97
- Samland M., et al., 2017, *A&A*, 603, A57
- Schlawin E., Agol E., Walkowicz L. M., Covey K., Lloyd J. P., 2010, *ApJL*, 722, L75
- Schneider J., Dedieu C., Le Sidaner P., Savalle R., Zolotukhin I., 2011, *A&A*, 532, A79
- Sheppard K. B., Mandell A. M., Tamburo P., Gandhi S., Pinhas A., Madhusudhan N., Deming D., 2017, *ApJL*, 850, L32
- Seager S., Sasselov D. D., 2000, *ApJ*, 537, 916
- Seager S., 2003, *ASPC*, 294, 457, *ASPC..294*
- Seager S., Deming D., Valenti J. A., 2009, *ASSP*, 10, 123

- Sedaghati E., et al., 2017, *Natur*, 549, 238
- Seidel J. V., et al., 2019, *A&A*, 623, A166
- Sing D. K., et al., 2012, *MNRAS*, 426, 1663
- Sing D. K., et al., 2015, *MNRAS*, 446, 2428
- Sing D. K., et al., 2016, *Natur*, 529, 59
- Slanger T. G., et al., 2005, *JGRD*, 110, D23302
- Smalley B., et al., 2012, *A&A*, 547, A61
- Smette A., et al., 2015, *A&A*, 576, A77
- Snellen I. A. G., Albrecht S., de Mooij E. J. W., Le Poole R. S., 2008, *A&A*, 487, 357
- Snellen I. A. G., de Kok R. J., de Mooij E. J. W., Albrecht S., 2010, *Natur*, 465, 1049
- Snellen I. A. G., et al., 2012, *SPIE*, 8444, 84440I, *SPIE*.8444
- Sotzen K. S., et al., 2020, *AJ*, 159, 5
- Spake J. J., et al., 2018, *Natur*, 557, 68
- Spake J. J., et al., 2019, *arXiv*, arXiv:1911.08859
- Spergel D., et al., 2015, *arXiv*, arXiv:1503.03757
- Strassmeier K. G., et al., 2015, *AN*, 336, 324
- Stevenson K. B., et al., 2014, *Sci*, 346, 838
- Stevenson K. B., et al., 2016, *PASP*, 128, 094401
- Strand K. A., 1943, *PASP*, 55, 29
- Struve O., 1952, *Obs*, 72, 199
- Suomi V. E., Limaye S. S., Johnson D. R., 1991, *Sci*, 251, 929
- Tinetti G., et al., 2016, *DPS*, 123.37
- Tody D., 1986, *SPIE*, 627, 733, *SPIE*..627
- Thompson S. J., et al., 2016, *SPIE*, 9908, 99086F, *SPIE*.9908
- Triaud A. H. M. J., 2018, *haex.book*, 2, *haex.book*
- Tull R. G., 1998, *SPIE*, 3355, 387, *SPIE*.3355
- Vidal-Madjar A., Lecavelier des Etangs A., Désert J.-M., Ballester G. E., Ferlet R., Hébrard G., Mayor M., 2003, *Natur*, 422, 143

- von Essen C., Mallonn M., Welbanks L., Madhusudhan N., Pinhas A., Bouy H., Weis Hansen P., 2019, *A&A*, 622, A71
- von Essen C., Mallonn M., Hermansen S., Nixon M. C., Madhusudhan N., Kjeldsen H., Tautvaišienė G., 2020, arXiv, arXiv:2003.06424
- Vogt S. S., et al., 1994, *SPIE*, 2198, 362, SPIE.2198
- Wakeford H. R., et al., 2013, *MNRAS*, 435, 3481
- Wakeford H. R., et al., 2017a, *Sci*, 356, 628
- Wakeford H. R., et al., 2017b, *ApJL*, 835, L12
- Wakeford H. R., et al., 2018, *AJ*, 155, 29
- Walker G. A. H., Bohlender D. A., Walker A. R., Irwin A. W., Yang S. L. S., Larson A., 1992, *ApJL*, 396, L91
- Welbanks L., Madhusudhan N., 2019, *AJ*, 157, 206
- Wertz O., Absil O., Gómez González C. A., Milli J., Girard J. H., Mawet D., Pueyo L., 2017, *A&A*, 598, A83
- West R. G., et al., 2016, *A&A*, 585, A126
- Wolszczan A., Frail D. A., 1992, *Natur*, 355, 145
- Wytttenbach A., Ehrenreich D., Lovis C., Udry S., Pepe F., 2015, *A&A*, 577, A62
- Yan F., Henning T., 2018, *NatAs*, 2, 714
- Wytttenbach A., et al., 2017, *A&A*, 602, A36
- Yung Y. L., et al., 2018, *Astrobiology*, 18, 10
- Žák J., Kabáth P., Boffin H. M. J., Ivanov V. D., Skarka M., 2019, *AJ*, 158, 120

## Appendix

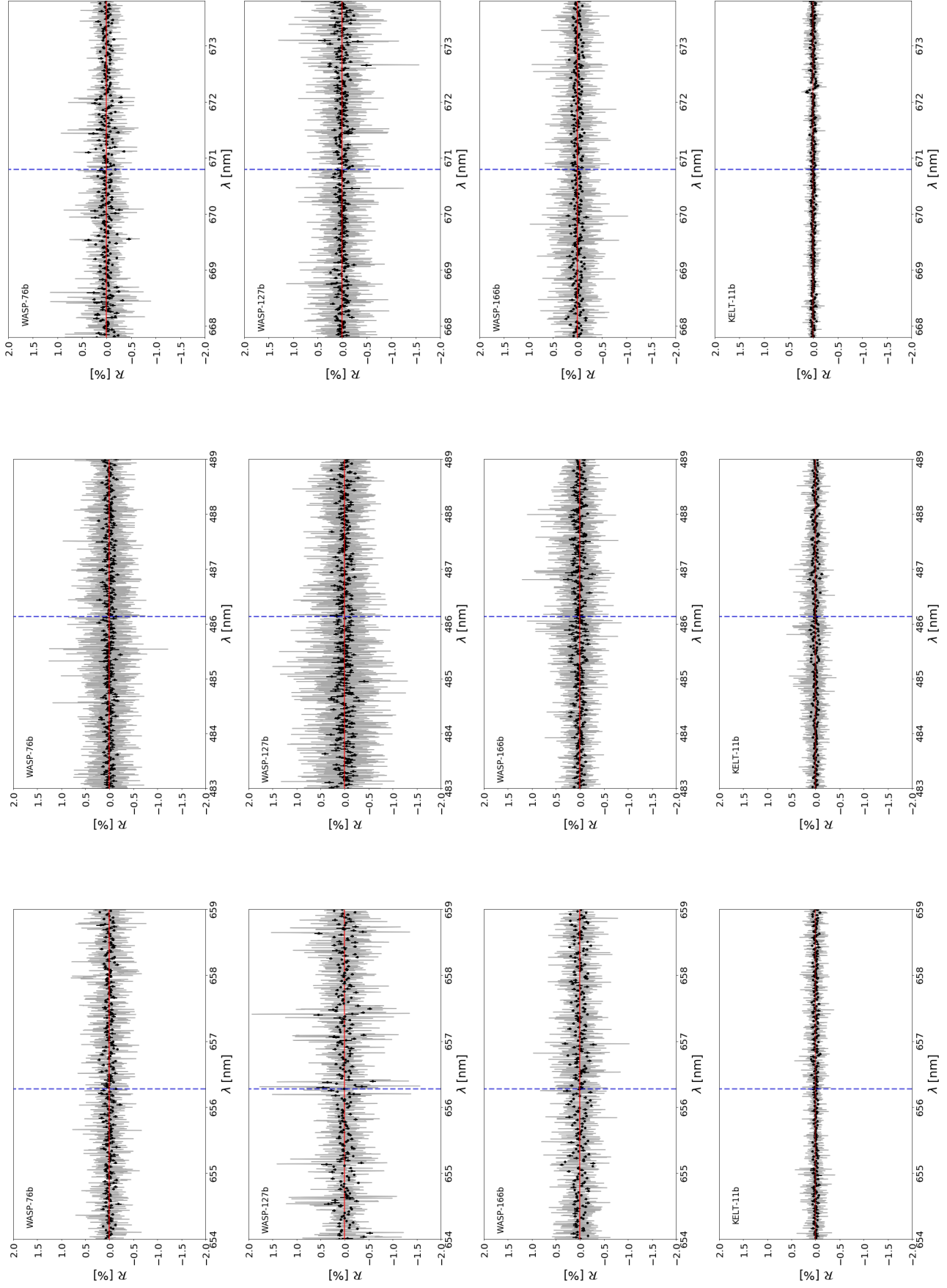


Figure A1: Spectral region around the H $\alpha$  line (left column), H $\beta$  (middle column) and lithium (right column). The final transmission spectrum (gray), binned spectrum by 20 (black) are shown. Blue dashed vertical lines show the expected position of planetary features. All subfigures show the non-detection of planetary features.

